Tectonophysics 764 (2019) 46–61

Contents lists available at ScienceDirect

Tectonophysics

journal homepage: www.elsevier.com/locate/tecto

Geodynamic effects of subducted seamount at the Manila Trench: Insights from numerical modeling

Zihua Cheng[a,b], Weiwei Ding[b,*], Manuele Faccenda[c], Jiabiao Li[b], Xiubin Lin[a], Letian Ma[b], Penggao Fang[a,b], Hanghang Ding[a,b]

[a] School of Earth Sciences, Zhejiang University 310027, Hangzhou, China
[b] Key Laboratory of Submarine Geosciences, State Oceanic Administration, Second Institute of Oceanography, Ministry of Natural Resources, 310012, Hangzhou, China
[c] Department of Geoscience, University of Padova, Via Gradenigo n. 6, 35131, Padova, Italy

ARTICLE INFO

Keywords:
Numerical modeling
Subducted seamount
Break-off
Manila Trench
South China Sea

ABSTRACT

We used numerical modeling to investigate the geodynamic effects of subducted seamounts at the Manila Trench. A series of numerical modeling experiments were conducted with variable parameters, including the activation volume (V_{act}) and cohesion (C), which influence lithospheric rheology, the plate convergence velocity, and the age of subducting slab. Modeling results indicate that varying the V_{act} and C within an appropriate range have limited effects on the geodynamic process of subduction. A lower V_{act} allows the slab to sink more easily and results in a steeper dip angle. A slab break-off is more likely to occur under subduction at depths of 100–300 km, while the existence of a seamount further promotes the break-off process. The convergence rate is a key parameter affecting the break-off timing and depth. In contrast, under subduction where subducted oceanic plate move faster upper plate, the model results exhibit non-break-off, steady subduction. Slab age is another factor controlling break-off, where break-off time extends with slab age. A subduction without seamount will cause a ~2 Myr delay in break-off timing. We suggest that the low-velocity zone under the Manila Trench at 17° N is the result of a break-off event due to subduction of the Zhenbei-Huangyan Seamount Chain. Further to the north, such as the location at 19° N, the absence of seamount and an older oceanic crust would favor a delay in break-off timing during subduction.

1. Introduction

Seamounts, oceanic ridges, and plateaus are common features that make oceanic crust inhomogeneous. Most of these structures follow plate movement and are ultimately recycled into the mantle at convergent margins, especially around the west Pacific margin. Seamount subduction appears to affect the slab morphology, topographic structure, volcanic arcs, as well as the degree of coupling between the overriding and subducting plates which may affect seismicity (Van Hunen et al., 2000, 2002; Lallemand et al., 2005; Livermore et al., 1997; McGeary et al., 1985). Furthermore, seamount (or seamount chain) subduction is responsible for the dramatic changes in the dynamics and kinematics of subduction zones (e.g.,Rosenbaum and Mo, 2011). Numerical and analogue modeling is an effective method in exploring the seamount subduction process and its role in convergent margins (Mason et al., 2010). Numerous modeling experiments have been carried out in recent decades to evaluate the geodynamic effects of subducted seamounts on slab dipping angle (Van Hunen et al., 2002; Espurt et al., 2008; Groome and Thorkelson, 2009; Taramon et al., 2015), slab break-off (van Hunen and Allen, 2011; Hu and Liu, 2016; Hu et al., 2016), collision patterns and volcanic activity (Gerya et al., 2009; Vogt and Gerya, 2014), and the topographic response of the upper plate (Dominguez et al., 1998, 2000; Martinod et al., 2005; Ding and Lin, 2016). However, previous studies on the effects of seamounts were performed under the conditions of an oceanic subduction model with either a fixed continental plate, or a slow convergence rate. This left considerable latitude for the geodynamics of seamount subduction during continental overthrusting to be addressed, such as at the Manila Trench in the eastern part of the South China Sea (SCS), where the Luzon Island is overthrusting over the SCS resulting from a NNW-trending motion towards the Eurasian Plate (EP). Seamount behavior in this dynamic situation remains enigmatic in terms of the physical factors controlling initiation, duration, and dynamics of the subduction.

In this study, we performed several thermo-mechanical modeling experiments to investigate the comprehensive scenarios during seamount subduction from initial collision to subsequent coupling with the

* Corresponding author at: Second Institute of Oceanography, Ministry of Natural Resource, Baochubei Road 36, Hangzhou 310012, China.
E-mail address: wwding@sio.org.cn (W. Ding).

https://doi.org/10.1016/j.tecto.2019.05.011
Received 22 November 2018; Received in revised form 30 April 2019; Accepted 9 May 2019
Available online 16 May 2019

mantle. Different parameters were re-considered during modeling works, including the lithospheric rheology, the convergence rate, and the slab age of the descending plate. Independent geophysical data from near ~17° N at the Manila Trench were compiled to provide realistic constraints on the modeling set-up, including the convergence rate between the SCS and the Luzon Island, the age of the SCS oceanic crust, the scale of the seamount chain, etc. The aim of our study is to model a classic, natural case considering the geodynamics features of a subducted seamount under continental overthrusting.

2. Geological setting

As one of the largest marginal basins in the western Pacific, the SCS has undergone nearly a complete Wilson cycle from continental rifting in latest Cretaceous to Paleogene, seafloor spreading in the early Oligocene-middle Miocene, and eastward subduction under the PSP starting in the early middle Miocene (i.e. Taylor and Hayes, 1983; Briais et al., 1993; Franke et al., 2014; Li et al., 2015; Sibuet et al., 2016). Based on magnetic anomaly interpretations, the seafloor spreading occurred between 32 and 16 Ma (Taylor and Hayes, 1983; Briais et al., 1993). Shipboard results of microfossil biostratigraphy and palaeomagnetic results from IODP Expeditions 349, 367& 368 (Li et al., 2014; Sun et al., 2018; Jian et al., 2018), combined with analysis on recently-acquired deep tow magnetic anomalies (Li et al., 2015), and $^{39}Ar/^{40}Ar$ dating of basement basalt near the fossil spreading ridge (Koppers, 2014), have shown that seafloor spreading occurred between ~33 Ma and 16 Ma, supporting the age model proposed by Taylor and Hayes (1983) and Briais et al. (1993).

Extensive magmatism occurred in the SCS basin after the cessation of seafloor spreading. Basaltic dating of dredged seamount samples ranges in ages from ~16 Ma to < 1 Ma (Wang et al., 2009; Expedition 349 Scientists, 2014). In this study we focused on the Zhenbei-Huangyan Seamount Chain in the center of the East Sub-basin, which is the most remarkable morphological relief generally developing along the fossil spreading ridge of the East Sub-basin (Briais et al., 1993; Li et al., 2015; Sibuet et al., 2016), and is experienced eastward subducting under the Luzon Island (see Fig. 1.b). It consists of several huge seamounts, including the Zhenbei seamount in the westmost, the Huangyan seamount in the middle, and a ~150 km long NEE-trending one in the far east which is connected with the Manila Trench. Geochemical analysis of the volcanic rocks suggested that the subduction of this seamount chain initiated at 5 Ma (Yang et al., 1996), and the subducted eastmost part extends northeastwards and reaches to 17–18° N under Luzon Island (Bautista et al., 2001). Dating of basaltic samples dredged from Zhenbei Seamount indicates an age range between 7.7 and 9.9 Ma (Wang et al., 2009). The crustal thickness of these seamounts is generally between 13 and 14 km based on a 3D deep seismic experiments in this area (He et al., 2016; Wang et al., 2016; Zhao et al., 2018).

Since 25 Ma, the PSP experienced a NNW movement with clockwise rotation (Wu et al., 2016), and collided with Mindoro in the middle Miocene (Hutchison, 2010). Continuous NNW motion finally triggered the collision between the Luzon Island and the EP at 8 Ma, as well as the orogeny of the Taiwan Island (e.g., Suppe, 1984; Huang et al., 2006). Wu et al. (2016) have reconstructed the subducted oceanic plate of the SCS based on results of seismic tomography, and they estimated the missing portion of the SCS (or the Manila slab) had extended to 124° E under the PSP. Previous regional and global tomographic studies (e.g., Lallemand et al., 2001; Wang et al., 2006; Zhao et al., 2013; Koulakov et al., 2014) presented the geometry of the subducted SCS, and have also suggested that the Manila slab varies its dip angles along the Manila Trench from north to south by ~25° between 18 and 21° N, 32° at 17° N, and nearly vertical at 14° N. The crustal thickness calculated from geophysical data shows that the thickness of the Luzon Island is between 25 and 29 km crust (Dimalanta and Yumul Jr., 2003). This result is consist with the Moho depth of 18–34 km reported by Besana et al. (1995). With the compilation of more recent data, the crustal thickness of the archipelago of Philippines ranges from 12 km to 32 km (Manalo et al., 2015), where a transition from continental to island arc terrane occurs.

Previous estimates of plate convergence rates between the PSP and SCS are between 80 and 100 mm/yr around 20° N, decreasing southwards to 50–60 mm/yr around 14° N (Kreemer et al., 2003; Sella et al., 2002). Simons et al. (2007) analyzed GPS data with a mapping strategy to obtain an accurate global plate velocity, and Hsu et al. (2012) refined the convergence rate along the Manila Trench as it progressively decreases southward from 91 mm/yr at the northern tip of Luzon Island to 55 mm/yr north of Mindoro.

3. Model set-up

3.1. Initial configuration

The numerical models were constructed with the thermo-mechanical code "I2VIS" (Gerya and Yuen, 2003, 2007) based on the finite difference method and marker-in-cell techniques. The model comprised three parts: (1) an oceanic crust with an attached seamount on the left; (2) a continental domain in the middle; and (3) another oceanic crust with a spreading ridge on the right. The seamount, along with the oceanic lithosphere on the left of the model, moved towards the continental domain and subducted under the continental margin. All oceanic domains comprised 3 km of basalt and 5 km of gabbroic rocks, with the lateral extent of 2380 km on the left and 1000 km on the right of the continent. The continental domain was felsic and had a total thickness of 30 km, consisting of 10 km upper crust and 20 km lower crust. For simplicity, we assumed that the composition of the seamount was similar to that of the oceanic domain, namely a basaltic and gabbroic lithology. The seamount had a total thickness of 16 km, which was subdivided into 8 km of upper and 8 km of lower oceanic crust, and a length of 150 km. These parameters are according to the scaling of the subducting seamount in the eastmost of the recent Zhenbei-Huangyan Seamount Chain. A weak zone was set to initiate subduction at the ocean-continent transition. The weak zone cut through the lithospheric mantle at an angle of 60° and was characterized by weak plastic strength (1 MPa) and wet olivine dislocation creep parameters (Ranalli, 1995).

The initial temperature field of the oceanic domain was defined by the oceanic geotherm for a half-space cooling model (Turcotte and Schubert, 2002). Embedded into the oceanic plate, the seamount was considered to have the same thermal structure. The initial temperature field of the continental domain increased linearly from 0 °C at the surface (20 km) to 1344 °C at the lithosphere-asthenosphere boundary (130 km depth). A thermal gradient of 0.5 °C was used for the asthenospheric mantle (> 130 km).

The leftward and rightward velocities, which refer to the absolute subduction velocity of the descending slab and the absolute trenchward velocity of the overriding continental plate, were internally prescribed at 1000 km and 3500 km, respectively, within the oceanic lithosphere (Fig. 2). In the reference model, the convergent velocity was set as 5 cm/yr according to Hsu et al. (2012). The left descending plate (R_L) was set to move rightwards with a velocity of 1 cm/yr, being consistent with a low velocity of the SCS obtained by Simons et al. (2007). The remaining −4 cm/yr was assigned to be the left overthrusting velocity (R_R) (Table 1). Different convergent rate were used in other models (MIII series, Table 2) to evaluate the effects of convergence rate on the development of slab geometry during seamount subduction.

3.2. Boundary conditions

All the boundaries are set to be free to slip, except for the lower boundary, which is permeable to satisfy free slip at an external boundary at 1400 km in the vertical direction (Gorczyk et al., 2007).

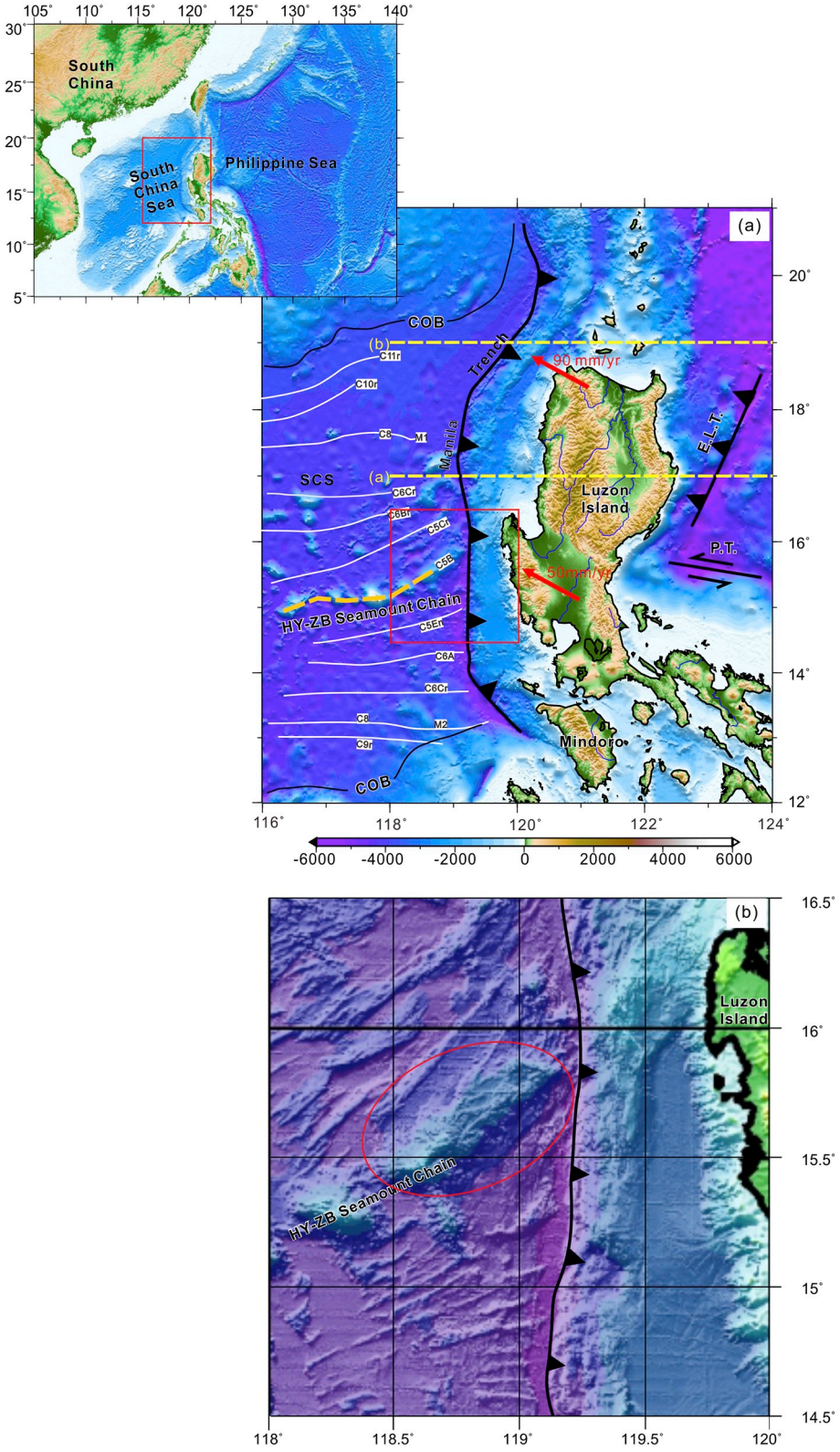

Fig. 1. (a), Morphological features along the Manila Trench and its adjacent regions. Yellow broken lines are the locations of P-wave tomographic sections. COB: continental-oceanic boundary (Li et al., 2015). P.T.: Philippine Trench; E.L.L.: East Luzon Trench; ZB-HY: Zhenbei-Huangya. Thick dashed orange lines represent the fossil spreading ridge. White solid lines are magnetic anomalies (Li et al., 2015). (b) A zoom in map of the subducting seamount of the ZB-HY Seamount Chain, The green circle represent Zhenbei and Huangyan seamounts, the red the circle represent the largest seamount of ZB-HY Seamount Chain. (For interpretation of the references to colour in this figure legend, the reader is referred to the web version of this article.)

External slip must conform to global conservation of mass in the computational domain and is implemented using the following limitation for velocity components at the lower boundary: $\partial \nu z/\partial z = -\nu z/\Delta z_{external}$, where $\Delta z_{external}$ is the vertical distance from the lower boundary to the external boundary such that free slip ($\partial \nu x/\partial z = 0$, $\nu z = 0$) is satisfied. To allow topographic build-up of the lithosphere, pseudo-free surface condition is imposed with a top surface layer (air for 20 km and a water layer for 2–4 km) characterized by low viscosity (10^{18} Pas) and low density (1 kg/m^3 for air, 1000 kg/m^3 for sea water).

3.3. Governing equations and numerical implementation

The momentum, continuity, and heat conservation equations for the two-dimensional creeping-flow, accounting for thermal and chemical

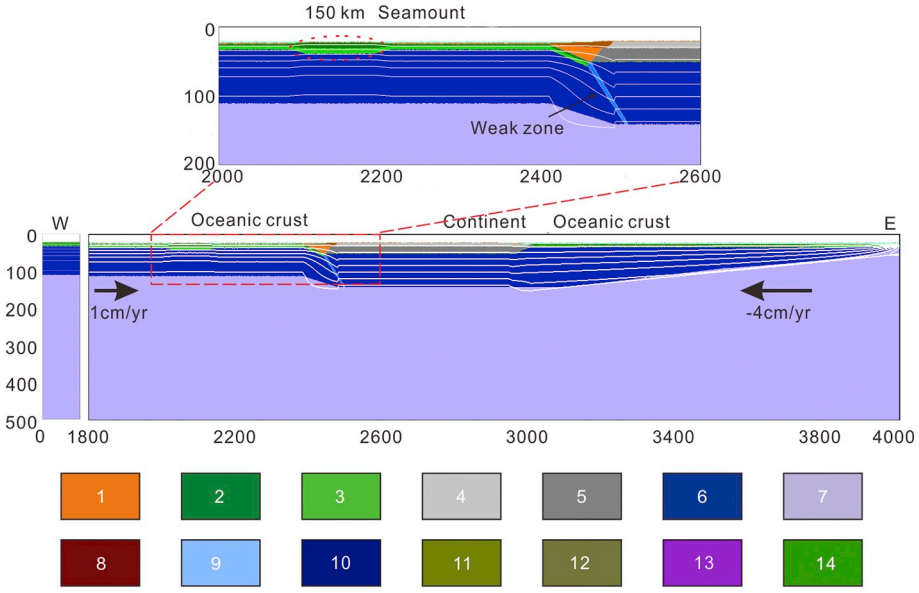

Fig. 2. Initial model setup. Full box initial geometry (4000 × 1400 km) and crop on the collision domain (700 × 200 km) with initial thermal structure. White lines are isotherms with an increment of 200 °C starting from 100 °C. Black arrows represent downgoing plate velocity (R_L) and right overthrusting velocity (R_R) respectively. Red dash circle encloses the seamount area. Colours indicate the materials that constitute different layers within the models. (1) Sediment, (2) gabbro, (3) basalt, (4) upper continental crust, (5) lower continental crust, (6) lithospheric mantle, (7) asthenospheric mantle, (8) partially molten mantle, (9) weak zone and wet mantle, (10) serpentinized mantle, (11) partially molten lower continental crust, (12) partially molten continental upper crust, (13) partially molten basalts, (14) new crust from molten material. (For interpretation of the references to colour in this figure legend, the reader is referred to the web version of this article.)

buoyancy, are solved using the modified I2VIS code (Gerya and Yuen, 2003, 2007). Conservation of mass is approximated by the incompressible continuity equation:

$$\frac{\partial v_x}{\partial x} + \frac{\partial v_z}{\partial z} = 0 \tag{1}$$

Two-dimensional Stokes equations:

$$\frac{\partial \sigma_{xx}}{\partial x} + \frac{\partial \sigma_{xz}}{\partial z} = \frac{\partial P}{\partial x} \tag{2}$$

$$\frac{\partial \sigma_{zz}}{\partial z} + \frac{\partial \sigma_{xz}}{\partial x} = \frac{\partial P}{\partial z} - g\rho(T,P,C) \tag{3}$$

and a heat conservation equation:

$$\rho C_p\left(\frac{DT}{Dt}\right) = -\frac{\partial q_x}{\partial x} - \frac{\partial q_z}{\partial z} + H_r + H_a + H_s + H_L \tag{4}$$

$$q_x = -k(T,C)\frac{\partial T}{\partial x},\ q_z = -k(T,C)\frac{\partial T}{\partial z} \tag{5}$$

$$H_r = constant\,(dependent\ on\ rock\ composition) \tag{6}$$

$$H_a = T\alpha\frac{DP}{Dt} \tag{7}$$

$$H_s = \sigma_{xx}\dot{\varepsilon}_{xx} + \sigma_{zz}\dot{\varepsilon}_{zz} + \sigma_{xz}\dot{\varepsilon}_{xz} \tag{8}$$

are used, where DT/Dt is the substantive time derivative of temperature $k(T,P,C)$; is the thermal conductivity as a function of temperature(T), pressure(P), and composition(C) (Hofmeister, 1999); Cp is the effective isobaric heat capacity, incorporating latent heat; H_r, H_a, and H_S denote radioactive heat production, the energetic effect of isothermal (de) compression (i.e., adiabatic heating/cooling), shear heating, and latent heating respectively.

3.4. Rheological model

Viscosity, dependent on strain rate, pressure, and temperature, is defined in terms of deformation invariants:

$$\eta_{creep} = =(\dot{\varepsilon}_{II})^{\frac{1-n}{2n}}A^{1/n} \times exp\left(\frac{E_a + V_aP}{nRT}\right) \tag{9}$$

$$\dot{\varepsilon}_{II} = 1/2\dot{\varepsilon}_{ij}\dot{\varepsilon}_{ij} \tag{10}$$

where $\dot{\varepsilon}_{II}$ is the second invariant of the deviatoric strain rate tensor; A, E_a, V_a, and n are the material constant, the activation energy, the activation volume, and the stress exponent respectively. These material properties were determined from laboratory flow experiments and are given in Table 1. Plasticity is implemented using the Druker-Prager yield criterion (Ranalli, 1995). The calculated creep viscosity is therefore limited as follows:

$$\eta_{creep} \le \frac{C + Psin(\varphi)}{(4\dot{\varepsilon}_{II})^{\frac{1}{2}}} \tag{11}$$

where C is the cohesion and φ is the internal angle of friction.

3.5. Partial melting and melt extraction

In the model, the mantle solidus is intermediate between the wet and dry peridotite solidi because of incomplete hydration. In natural case, variable hydration triggers melting over a range of temperatures. Therefore, it is assumed that the degree of both hydrous and dry melting is a linear function of pressure and temperature (e.g., Gerya and Yuen, 2003). For a given pressure and rock composition, the volumetric degree of melting M_0 is:

$$M_0 = 0 \text{ when } T < T_{\text{solidus}} \tag{12}$$

$$M_0 = (T - T_{\text{solidus}})/(T_{\text{liquidus}} - T_{\text{solidus}}) \text{ when } T_{\text{solidus}} < T < T_{\text{liquidus}} \tag{13}$$

$$M_0 = 1, \text{ when } T > T_{\text{liquidus}} \tag{14}$$

where T_{solidus} and T_{liquidus} are, respectively, the solidus temperature (wet and dry solidi are used for the hydrated and dry mantle, respectively) and the dry liquidus temperature at a given pressure and rock composition. However, melt may collect in channels or dykes and leave the melting zone (Schmeling, 2006, 2010). Following previous studies, a pre-defined melt threshold (e.g., Schmeling, 2010) is $M_{\max} = 4\%$, and a non-extractable amount of melt $M_{\min} = 2\%$ will remain in the source (e.g., Nikolaeva et al., 2008; Sizova et al., 2010). The amount of extracted melt during the evolution of an experiment is tracked by markers. The total amount of melt M for every marker takes into account the amount of previously extracted melt and is calculated as

$$M = M_0 - \sum_n M_{ext} \tag{15}$$

where $\sum_n M_{ext}$ is the total melt fraction extracted during the previous n extraction episodes. Rocks are considered refractory when the extracted melt fraction is larger than the standard one (i.e. when $\sum_n M_{ext} > M_0$). If the total amount of melt exceeds the threshold $M_{\max}$, the melt fraction $M_{\text{ext}} = M - M_{\min}$ is extracted and $\sum_n M_{ext}$ is updated. Extracted melts

Table 1
Material properties used in the two-dimensional numerical experiments.

Material	State	ρ_0 (kg m^{-3})	k (W m^{-1} K^{-1})	H_r (μW m^{-3})	Viscous Flow law	Plastic Sin(φ_{eff})	P-T conditions of solidus (K)	P-T conditions of liquidus (K)
Sediment	Solid	2700	0.64 + 807/(T + 77)	1.5	Wet quartzite	0.15	889 + 17,900/(P + 54) + 20,200/(P + 54)^2, at P < 1200 MPa;	1262 + 0.009P
	Molten	2500					831 + 0.06P, at P > 1200 MPa	
Continental upper crust	Solid	2700	0.64 + 807/(T + 77)	1.0	Wet quartzite	0.15	889 + 17,900/(P + 54) + 20,200/(P + 54)^2, at P < 1200 MPa;	1262 + 0.009P
	Molten	2500					831 + 0.06P, at P > 1200 MPa	
Continental lower crust	Solid	3000	0.64 + 807/(T + 77)	0.25	Plagioclase_An75	0.15	889 + 17,900/(P + 54) + 20,200/(P + 54)^2, at P < 1200 MPa;	1423 + 0.105P
	Molten	2500					831 + 0.06P, at P > 1200 MPa	
Upper Oceanic crust	Solid	3000	1.18 + 474/(T + 77)	0.25	Wet quartzite	0.15	973–70,400/(P + 354) + 778 × 10^5/(P + 354)^2, at P < 1600 MPa;	1423 + 0.105P
	Molten	2900					935 + 0.0035P + 0.0000062P^2, at P > 1600 MPa	
Lower oceanic Crust	Solid	3000	1.18 + 474/(T + 77)	0.25	Plagioclase_An75	0.6	973–70,400/(P + 354) + 778 × 10^5/(P + 354)^2, at P < 1600 MPa;	1423 + 0.105P
	Molten	2900					935 + 0.0035P + 0.0000062P^2, at P > 1600 MPa	
Mantle	Dry	3300	0.73 + 1293/(T + 77)	0.022	Wet_olivine	0.6	–	
	Hydrated	3200				0.06		
References	–	bb[a,b]	bb[c]	A	bb[d]	–	bb[f]	

[a] Turcotte and Schubert, 2002.
[b] Bittner and Schmeling, 1995.
[c] Clauser and Huenges, 1995.
[d] Ranalli, 1995.
[f] Schmidt and Poli, 1998.

Table 2
Main parameters used in models; V_{act}-m is the mantle volume activation, $V_{ac}t$-o is oceanic crust volume activation, C is cohesion, R_L is the left downgoing plate velocity, and R_R is the right overriding plate velocity. Age is the oceanic crust age. MVI-1* is with oceanic upper plate, and the age is 100 Ma (See in supplementary material Fig.S1).

Model	V_{act}-m(J/bar)	V_{act}-o (J/bar)	C(MPa)	R_L/R_R(cm/yr)	Age(Ma)
M I-1	1.1	0.8	10	1/−4	20
M I-2	1.1	1.1	10	1/−4	20
M I-3	0.8	0.8	10	1/−4	20
M II-1	1.1	0.8	1	1/−4	20
M II-2	1.1	1.1	1	1/−4	20
M II-3	0.8	0.8	1	1/−4	20
M III-1	1.1	0.8	10	1/−6	20
M III-2	1.1	0.8	10	1/−8	20
M III-3	1.1	0.8	10	1/−2	20
M III-4	1.1	0.8	10	1/−1	20
M III-5	1.1	0.8	10	4/−1	20
M III-6	1.1	0.8	10	6/−1	20
M IV-1	1.1	0.8	10	1/−4	30
M IV-2	1.1	0.8	10	1/−4	40
M IV-3	1.1	0.8	10	1/−4	60
M V-1[a]	1.1	0.8	10	1/−4	20
MVI-1*	1.1	0.8	10	1/−4	20

are thought to leave the melting zone much faster when compared to rock deformation timescales (Elliott et al., 1997; Hawkesworth et al., 1997). Thus, extracted melts are transmitted instantaneously to emplacement areas in the form of plutons and volcanics located right above the partial melting regions.

4. Model results

A reference model (MI-1) was established and run with geophysical constraints to simulate the subduction process of the Zhenbei-Huangyan Seamount Chain at ~16° N under the Manila Trench. To ascertain the impact of seamount subduction, we conducted another 15 models by modifying the activation volume (V_{act}) (MI-2, MI-3), the cohesion (C) of oceanic lithosphere (MII series), the convergence rate (MIII series), the slab age (MIV series), and a special case without the seamount (MV-1) (Table 1). We grouped the modeling results into four parts to evaluate the influence of the rheology, velocity, coupling, and external kinematic conditions.

4.1. Reference model development

As mentioned in model set-up, the reference model (MI-1) for seamount subduction is driven by a pushing force with a velocity of 1 cm/yr on the left and −4 cm/yr on the right (minus indicates a leftward moving direction). The activation volume (V_{act}) is 1.1 for the mantle and 0.8 for the oceanic crust, with a cohesion (C) of 10 MPa (Table 2).

As the continental domain moves trenchward with a velocity of −4 cm/yr, the oceanic domain on the left begins its subduction under the continental domain with a steep angle, which might be caused by the imposed angle of the weak zone (Fig. 3a). After 4.89 Myr, the seamount enters into the subduction channel and approaches the mantle-crust interface at ~10 Myr. The positive buoyancy force related to the seamount shallows the slab dip slightly, and water is released from the descending slab because of sediment compaction and mineral dehydration reactions (Fig. 3b). This stage is manifest as fluids percolating into the overlying mantle, which may form a serpentinized channel at shallow mantle-crust interfaces (about 100 km) or generate sub-solidus metasomatism at greater depths. Such fluids induce partial melting and enable basaltic melt production which will migrate upward along the slab top. During this stage, necking occurs in the subducted slab at the front margin of the seamount, which is finally broken off at a depth of about 237.5 km (after 10.72 Myr, Table 3). After this break-off

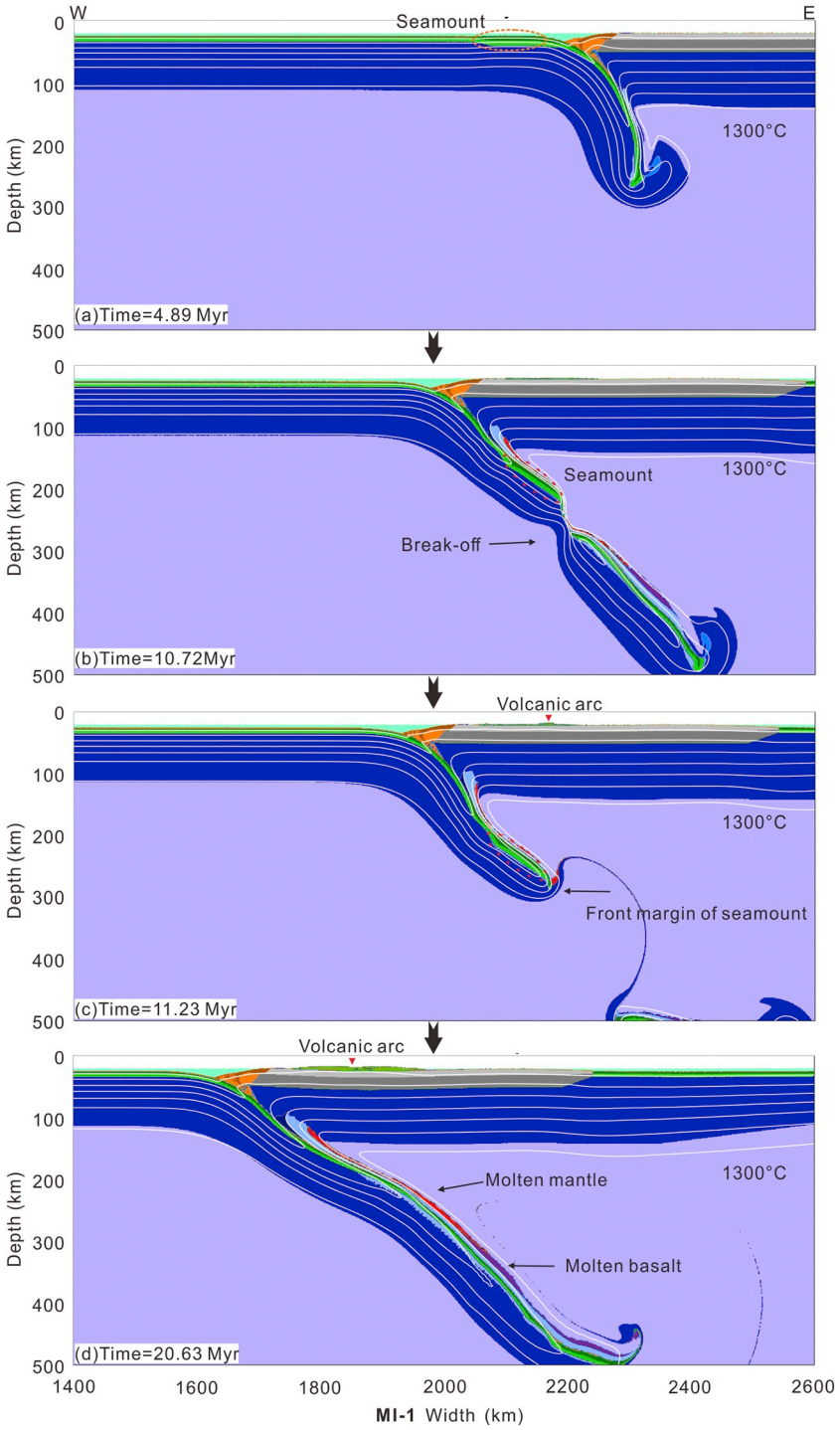

Fig. 3. Evolution of the compositional field for the reference model (MI-1). Water released from the downgoing slab lowers the melting temperature of the overlying mantle and allows for partial melting of the mantle. Break-off occurred at front margin of seamount. The down direction arrows represent model evolution order. The red triangle represents the location of volcanic arc. (For interpretation of the references to colour in this figure legend, the reader is referred to the web version of this article.)

event, the detached slab sinks rapidly into the mantle, and the subducted slab rebounds with slightly decreased dip angle (Fig. 3c). As the leftward movement of the continental domain, the slab continues its subduction. In areas where the extent of partial melting is sufficient to allow extraction, melts are emplaced at crustal levels to form plutons with extrusive volcanics on the overriding plates (Fig. 3d).

4.2. Influence of oceanic crust and mantle activation volume

Based on previous studies, an appropriate range of activation was chosen to prevent stagnant subduction formation (Crameri et al., 2012; Crameri and Tackley, 2015). In models MI-2 and MI-3, we modified the V_{act} (Table 2) of either the oceanic crust or the mantle to evaluate the ability of the slab to sink into the mantle.

In model MI-2, we increased the V_{act} of the oceanic crust from 0.8 J/bar to 1.1 J/bar, which yields higher viscosities with increasing depth.

Table 3
Influences of different parameters (see in Table 2).

Model	Break-off time[a] (Myr)	Break-off depth[b] (km)	Slab angle (*syn*-breakoff)	Slab angle[c] (post-breakoff)	Subducted slab length(km)[d]	Partial melting
M I-1	10.72	237.5	32.92	28.23/44.78	536	Yes
M I-2	10.62	178	37.70	33.53/51.35	531	Yes
M I-3	10.10	274.5	61.72	63.16	505	No
M II-1	10.62	186.4	33.84	25.13/47.54	531	Yes
M II-2	10.78	248.5	36.48	38.55/44.90	539	Yes
M II-3	10.29	285.6	65.86	61.30	514	No
M III-1	7.56	156.3	34.73	50.67	508.2	Yes, weak
M III-2	5.86	158.3	33.75	79.66	504.9	No
M III-3	20.21	252.5	45.33	25.23/42.00	600	Yes (intensive)
M III-4	/	/	/	28.83/37.49		Yes (intensive)
M III-5	/	/	/	–		No
M III-6	/	/	/	–		No
M IV-1	12.54	241.5	35	35.86/44.83	625	Yes
M IV-2	13.47	297.6	36.97	37.85/38.68	660	Yes
M IV-3	/	/	/	24.11/45.41		Yes
M V-1	13.08	251.5	28.47	20.78/41.10	654	Yes
MVI-1*	12.20	227.3	30.30	31.86/43.66	610	Yes

[a] Break-off time means the moment of complete separation of the detached slab from the rest subducted slab.
[b] Break-off depth means the depth where the breakoff takes place.
[c] Two numbers mean a kink structure, representing the angle of the upper part and lower part respectively.
[d] Subducted slab length is simply defined by multiplying convergence rate of two plate and Break-off time.
* Model with a oceanic upper plate, details shown in Table 2.

In contrast with the reference model, in model MI-2 a higher V_{act} of the oceanic crust makes the slab resistant to bending in the mantle. The dip angle of the slab is shallower (Fig. 4a-1), and the break-off occurs near the back margin of the seamount (Fig. 4a-2). After the break-off event the detached slab sinks quickly into the mantle (Fig. 4a-3), and the oceanic crust keeps subducting with a dip angle of 33.5°, which increases to 51.3° further downward (Table 3, Fig. 4a-4).

In contrast, we decreased the V_{act} of the mantle from 1.1 J/bar to 0.8 J/bar in model MI-3. Modeling results indicate that the slab sinks into the mantle more easily than in the reference model and presents as a higher dip angle of nearly 69°. Slab drip-off first occurs after the seamount chain enters the subduction channel at 6.8 Myr (Fig. 4b-1). With the continuous leftward movement of the continental domain, the seamount is entirely subducted into the mantle, and the break-off occurs at the front margin of the seamount (Fig. 4b-2). It is noteworthy that the break-off occurs at 10.10 Myr, which is slightly earlier than in models MI-1 and MI-2 (10.55 Myr and 10.72 Myr, respectively). The detached slab also sinks into the mantle quickly (Fig. 4b-3), and the following slab maintains stable subduction for about 5 Myr with a dip angle of 63.1° before a second break-off occurring at the back margin of the seamount chain near a depth of 400 km. Compared with the reference model (MI-1) and the model with high V_{act} (MI-2), model MI-3 with V_{act} of 0.8 J/bar is characterized by less melting and volcanic activity in the upper plate, and a higher slab dip angle.

4.3. Influence of cohesion

Models MII-1, MII-2, and MII-3 were set to evaluate the influence of cohesion during seamount subduction. Cohesion(C) is a key parameter reflecting lithospheric strength (Ranalli, 1995). The higher C is, the stronger the lithosphere is.

When C is decreased to 1 MPa (Table 2), our results show different features (MI series). For models with relatively high V_{act} (MII-1, MII-2), there is more oceanic crust melting at depths between 300 and 400 km than in models MI-1 and MI-2 with the cohesion of 10 MPa, especially after the slab break-off. Both Fig. 5a and b show higher volcanic activities at the surface of the overriding plate, which indicates a large amount of melting. Two volcanic arcs can be distinguished at the surface of the continental domain. The first one occurs in the central part of the continental domain surface, forms shortly after the occurrence of slab break-off, and is characterized by ~100 km widths. Another volcanic arc forms after the sinking of the detached slab near the trench (about 50 km), although the scale is much smaller than in the first arc (Fig. 5a and b). These two volcanic arcs keep increasing as slab subduction continues.

However, the result of model MII-3 with low activation volume shows limited melting, and no volcanic activities are observed on the surface of the continental domain. The dip angle of the subducted slab reaches up to ~60°, which is much higher than those of models MII-1 and MII-2, but is very similar to model MI-3 (Fig. 5c and Fig. 4b).

4.4. Influence of convergence rate

Subduction rate and slab length are strongly dependent on the ratio between the rightward velocity of the oceanic plate (R_L) and leftward velocity of the continental domain (R_R). Models MIII-1 to MIII-6 (Table 2) were designed to investigate the effect of the convergence rate on the slab geodynamic features during subduction. For models MIII-1 and MIII-2, we increased the R_R to 6 cm/yr and 8 cm/yr, respectively.

Compared with the reference model MI-1, the higher R_R does not significantly change the subduction dynamics (Fig. 6a and b), except for the timing and depth of the slab break-off event. The results of model MIII-1 show that the slab detaches after 7.56 Myr of subduction, and the break-off event occurs at the back margin of the seamount at a depth of ~156 km, whereas in the reference model MI-1, the detached time of the slab is after 10.72 Myr, and the break-off event occurs at the front margin of the seamount (Fig. 3). After the sinking of the detached slab and the ongoing subduction, a drip-off occurs at a depth of ~450 km (Fig. 6a-3).

Model MIII-2 has a higher overriding plate rate of 8 cm/yr, and the results show that the break-off occurs much earlier than that in model MIII-1 (5.86 Myr compared with 7.56 Myr, Fig. 6a-2 and 6b-2), as well as the occurrence of drip-off (9.19 Myr compared with 14.04 Myr, Fig. 6a-3 and 6b-3). The drip-off depth is also much shallower.

However, for model MIII-3 with a low R_R (2 cm/yr, Table 2), slab drip-off occurs first after 14.3 Myr of subduction, while the break-off event occurs much later at the back margin of the seamount (20.21 Myr, Fig. 7a). For model MIII-4, with extremely low R_R (1 cm/yr, Table 2), the drip-off occurs much later (19.98 Myr), and no break-off event happens, except a slab necking after 37.96 Myr at a depth of

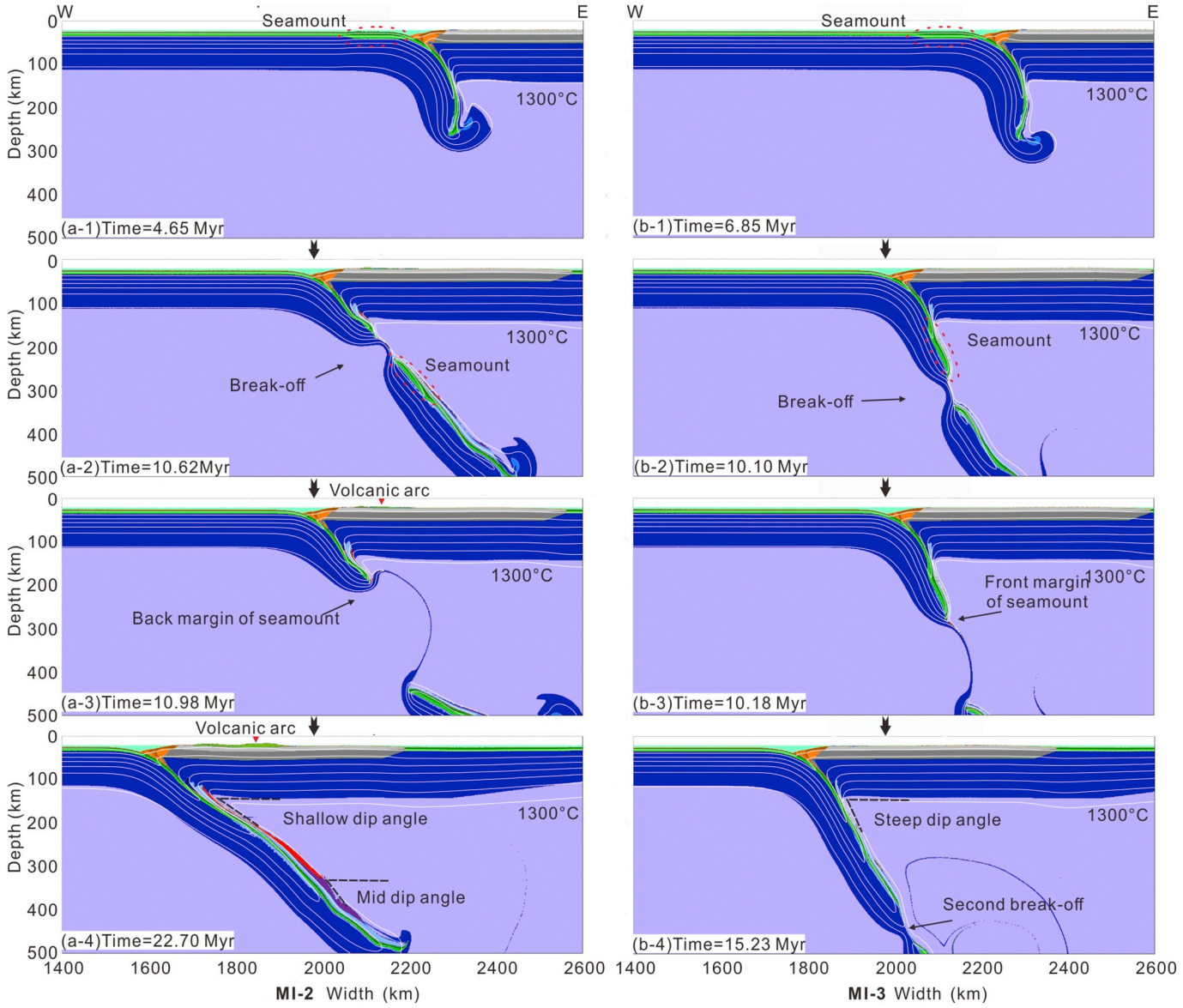

Fig. 4. Evolution of the compositional field for different activation volume (M1-2 and M1-3). (a) is a V_{act} of 1.1 for both oceanic crust and mantle; (b) is a V_{act} of 0.8 for both.

~450 km (Fig. 7b). The amount of volcanic activity is voluminous in both models MIII-3 and MIII-4, since a low convergence rate allows enough time for partial melting.

In summary, both the break-off and drip-off timing is much later than those with high convergence velocity, even without break-off event.

Two models (MIII-5 and MIII-6) that were dominated by oceanic subduction were carried out for comparison. The R_L was set as 6 cm/yr and 8 cm/yr, while R_R was set at only 1 cm/yr. The results show that the oceanic domain subducts along the weak zone with a high dip angle 80° (Fig. 8a-1, 8b-1). The slab becomes almost vertical and subsequently folds and thickens at the 660-km discontinuity (Fig. 8a-2,3, 8b-3,3). Neither slab break-off nor necking occurs during subduction.

4.5. Influence of slab age

The MIV model series were set to evaluate the role of slab age on the seamount subduction process. The age of the left oceanic domain was set as 30 Ma for MIV-1, 40 Ma for MIV-2, and 60 Ma for MIV-3, respectively. The modeling experiments indicate that during the early stage of subduction, the dip angle of the slab increases with the age of the slab, which is ~70° for 30 Ma (Fig. 9a-1), ~80° for 40 Ma (Fig. 9b-1), and almost vertical for 60 Ma (Fig. 9c-1). The break-off event occurs at the back margin of the seamount in MIV-1 and MIV-2, but the timing is after 12.54 Myr and 13.47 Myr, respectively, which is later than that of the reference model (i.e., 10.72 Myr). After the sinking of the detached slab, all models show stable subduction with shallowing dip angles. In model MIV-3, no break-off event is observed, and the slab subducts stably (Fig. 9c-3).

4.6. Subduction without seamount

Model MV-1 was conducted to investigate the subduction process without a seamount in the left oceanic domain. Similar to the reference model (MI-1), a slab break-off occurs due to the young age of the oceanic lithosphere (Fig. 10a). However, the detachment time is delayed by about 2 Myr, and the depth is 13 km deeper (Tables 3, 13.08 Myr at 251 km in MV-1 vs. 10.76 Myr at 237.5 km in MI-1). After the break-off event, the slab begins to rebound because of the suction force caused by the continent's trenchward motion. As subduction

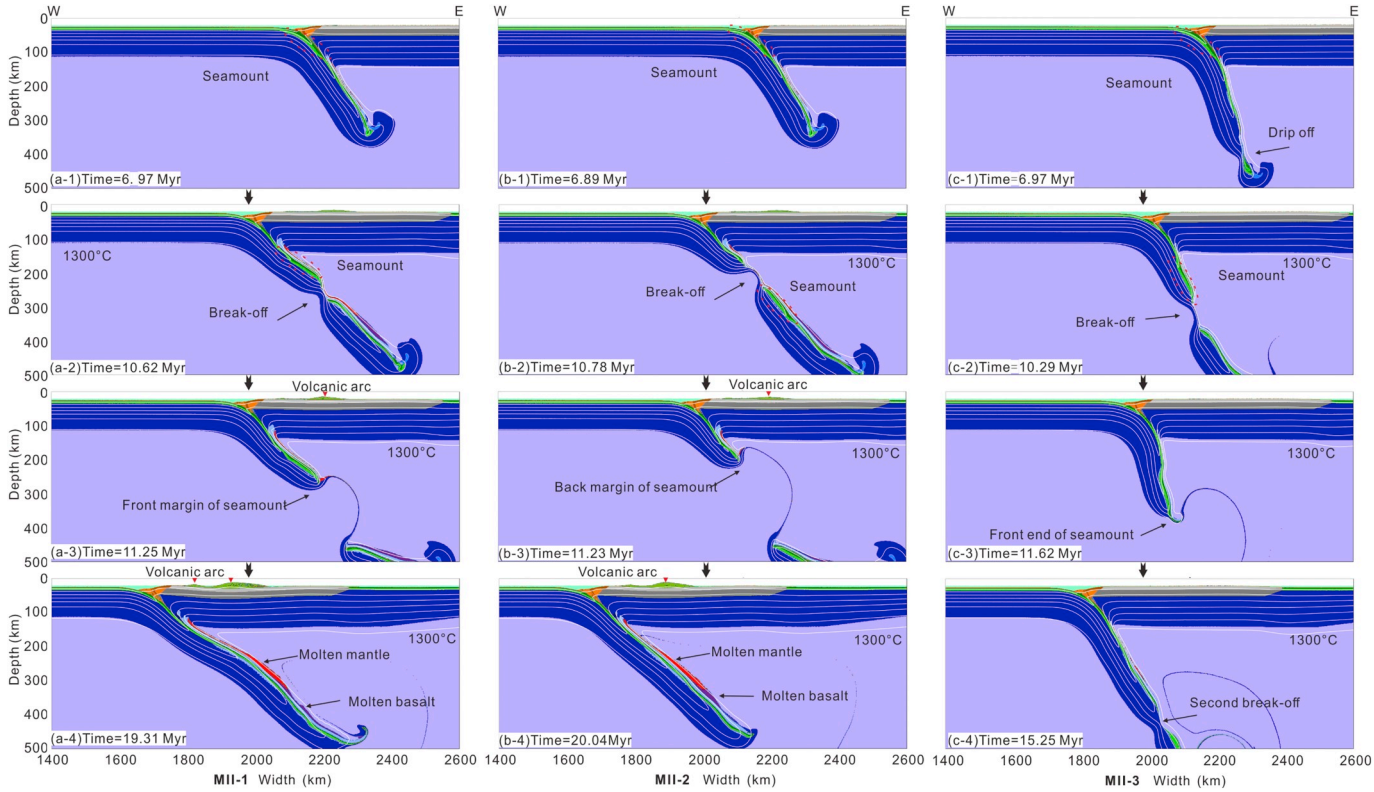

Fig. 5. Influence of lower cohesion (1 MPa) for different V_{act}. (a) MII-1, V_{act} is 0.8 for oceanic crust and 1.1 for mantle (b) MII-2, V_{act} is 1.1 for both oceanic crust and mantle (c) MII-3, V_{act} is 0.8 for both.

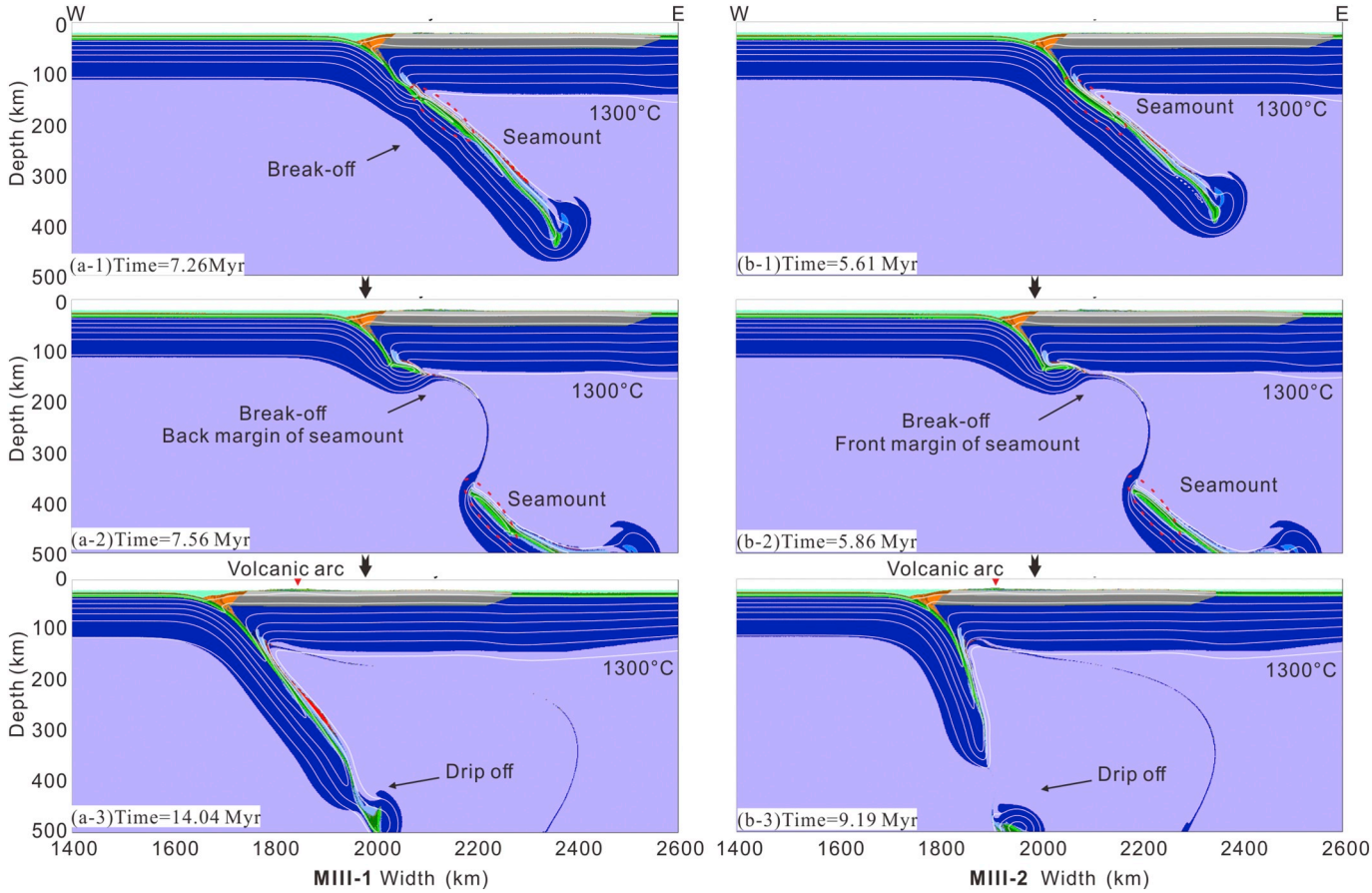

Fig. 6. Numerical modeling with high velocity of the overriding plate: (a) MIII-1: the rate of both plate is 1/−6 cm/yr; (b) MIII-2: 1/−8 cm/yr.

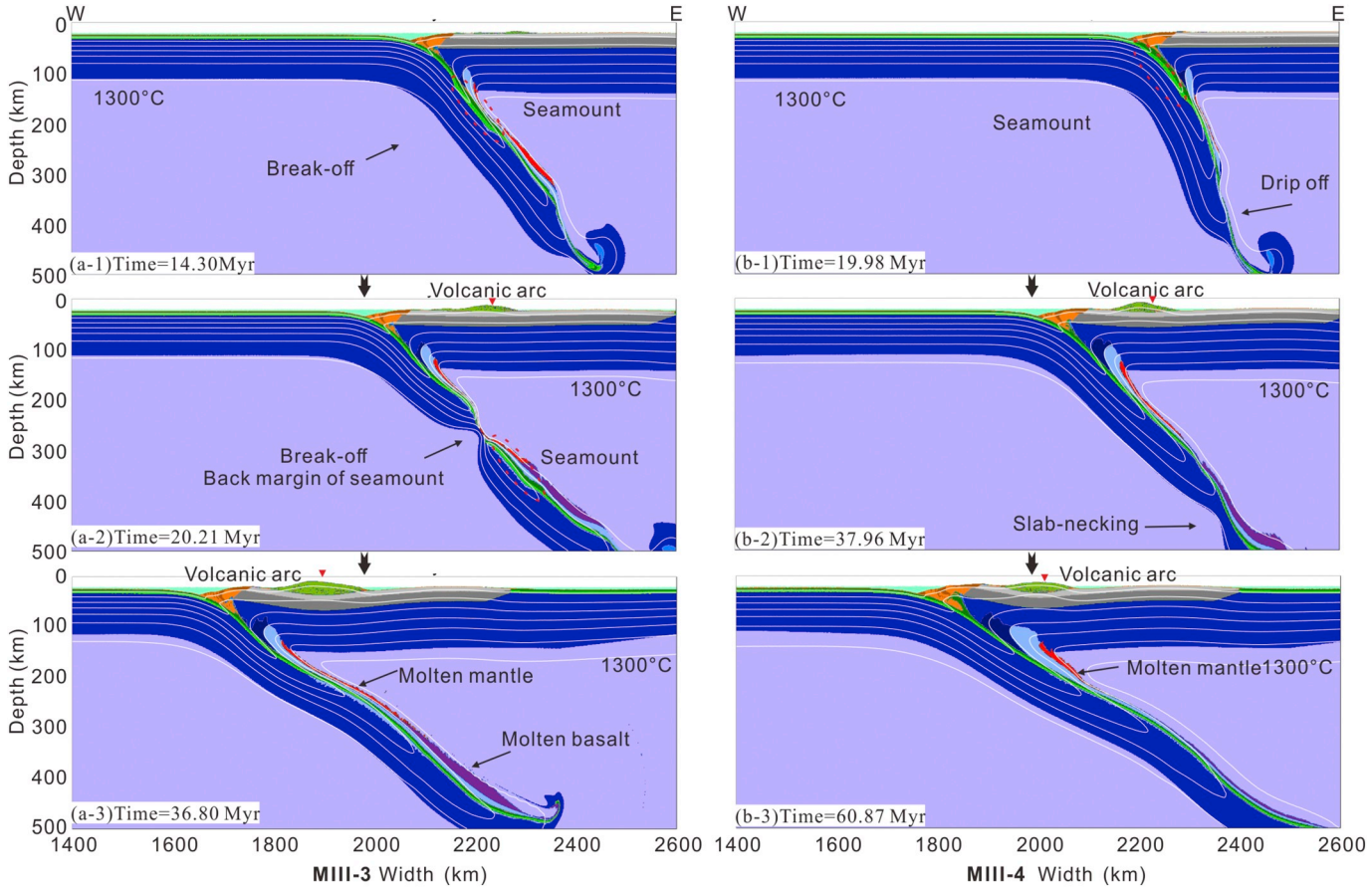

Fig. 7. Numerical modeling with low velocity of the overriding plate: (a) MIII-3: 1/−2 cm/yr; and (b) MIII-4: 1/−1 cm/yr.S

continues (Fig. 10b), flat subduction is established, characterized by eastward mantle flow beneath the slab. This stage lasts about 3 Myr, and is associated with large volumes of partial melting in the mantle. The flat slab increases its dip angle again below a depth of 300 km because of the negative buoyancy associated with the eclogitized oceanic crust (Fig. 10d).

5. Discussion

Slab break-off is common under collision zones based on seismic tomography analysis(e.g., Liu and Stegman, 2011; Wortel and Spakman, 2000), surface magmatism (e.g. Humphreys, 1995; Ferrari, 2004; Qin et al., 2008), uplift of the orogeny in the foreland (e.g. Wilmsen et al., 2009), etc. In general, a slowdown of the subduction rate is very possibly a causative mechanism, which can be achieved by ridge subduction or subduction of buoyant material. This slowdown rate could result in extensional stress within the downgoing plate (e.g., Huw Davies and von Blanckenburg, 1995; Yoshioka and Wortel, 1995; Duretz et al., 2011). According to our modeling results, slab break-off event occurs in 12 of the 16 total cases, except in models dominated by: (1) sustained oceanic subduction (models MIII-5 and MIII-6), which would create a continuous stress field within the slab; (2) extremely low convergence rates (model MIII-4), which would lower the stresses needed for the slab break-off; or (3) old slab ages (model MIV-3), which causes the slab to stiffen. This indicates that the slab break-off event is also a common feature during seamount chain subduction under continental overthrusting.

5.1. Rheology

Previous numerical experiments have proved that slab break-off timing and depth are strongly dependent upon rheology, i.e., low values of V_{act} (< 1.1 J/Pa) (Crameri et al., 2012; Crameri and Tackley, 2015), or low standard strength C (1 MPa) (Duretz and Gerya, 2013) will reduce the yield stress within the slab, and therefore result in rapid slab sinking and a break-off event.

The MI and MII model series were set to evaluate the role of rheology as indicated by variable activation volume and cohesion, while maintaining consistent convergence rate and slab age. Slab break-off was observed in all these models, indicating that a low V_{act} (≤1.1 J/Pa) and C (≤10 MPa) does favor a slab rupture. A change in either V_{act} or C does not change the break-off process significantly. However, the V_{act} of the oceanic crust mostly affects the break-off position and partial melting. A higher V_{act} of the oceanic crust results in a break-off at the back margin of the seamount chain. In contrast, as shown in models MI-3 and MII-3, a lower V_{act} of the mantle causes the subducted slab to sink into the mantle more vertically, because the mantle viscosity is relatively low and provides less resistance to subduction. Partial melting is limited during such a high-angle subduction, since the subducted slab sinks into the mantle rapidly and thermal heating of the slab is of insufficient duration to reach the dehydration and melting temperatures.

5.2. Convergence rate

Regarding the convergence rate during seamount subduction when upper plate move faster than downgoing plate, our model results suggest two different subduction types. Firstly, when the velocity of the overriding plate is higher than that of the downgoing plate, a slab break-off will occur. Advancing continent motion is generally associated with a low slab dip (Lallemand et al., 2005), while a young oceanic plate (20 Ma) also tends to result in low subduction angles due to its positive buoyancy (Duretz et al., 2011), which in turn enhances

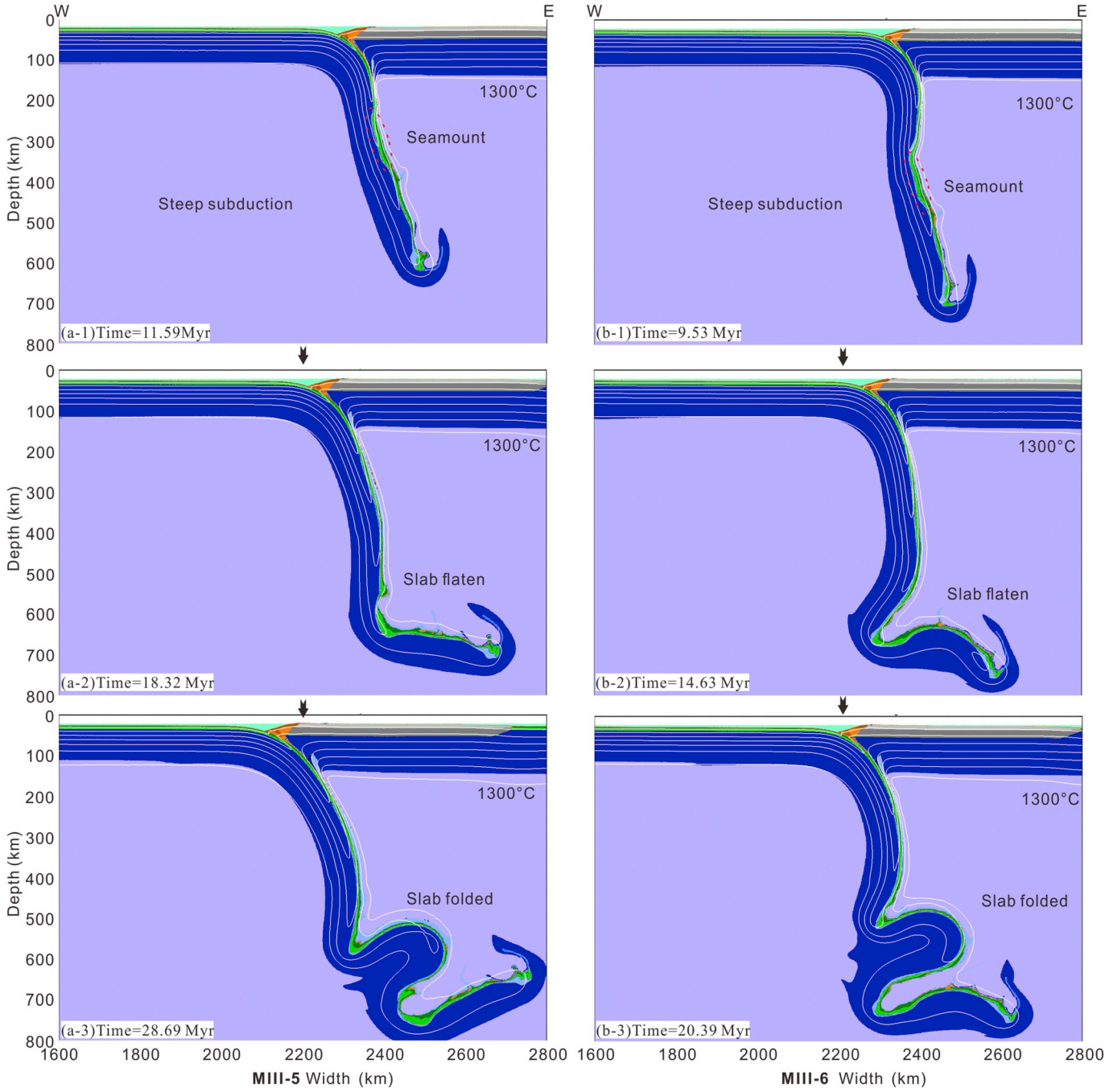

Fig. 8. Numerical modeling under oceanic subduction. (a) MIII-5: $R_L/R_R = 4/-1$ cm/yr; (b) MIII-6: $R_L/R_R = 6/-1$ cm/yr.

interplate pressure. As the slab subducts, it will gradually be 'anchored' into the underlying mantle, and fast-moving trench would increase the amount of extensional stresses within the slab by pulling the upper portion oceanwards. Therefore, the tectonic stresses tend to accumulate within the downgoing plate, causing necking and subsequent slab break-off. A much higher overriding continental domain velocity ($R_R \geq 6$ cm/yr) tends to induce a slab break-off event immediately after the seamount enters the mantle, and results in small-scale slab flattening (Fig. 6a-1, 6b-1). Secondly, in contrast, a lower rate (MIII-3, $R_R = 2$ cm/yr) would decrease extensional stresses within the slab on the oceanward upper portion due to slow-moving trench. Slow subduction allows the slab to be heated for a longer time by the surrounding mantle, which will induce slab drip-off and more melting, as well as a delayed break-off event (Fig. 7a, b). When the R_R is extremely low (1 cm/yr), as shown in model MIII-4, slab necking occurs because of the weakening of the slab by thermal diffusion.

On the contrary, a steady subduction without slab break-off events is observed when the downgoing plate is moving faster than the overriding plate (MIII-5 and MIII-6 models, Fig. 8). In this case, the oceanic domain subducts more freely with a steep angle (80°, Fig. 8), sinks rapidly into the lower mantle, and flattens and folds at a depth of 660 km. Since the primary requirement for a break-off is the development of extensional stresses within the descending plate (van Hunen and Allen, 2011), a fast oceanic domain subduction would counteract the slab pull caused by its negative buoyancy, such that extensional strain does not accumulate easily and prevents the occurrence of necking or slab rupture.

We calculated the dip angles and subducted slab length of all models

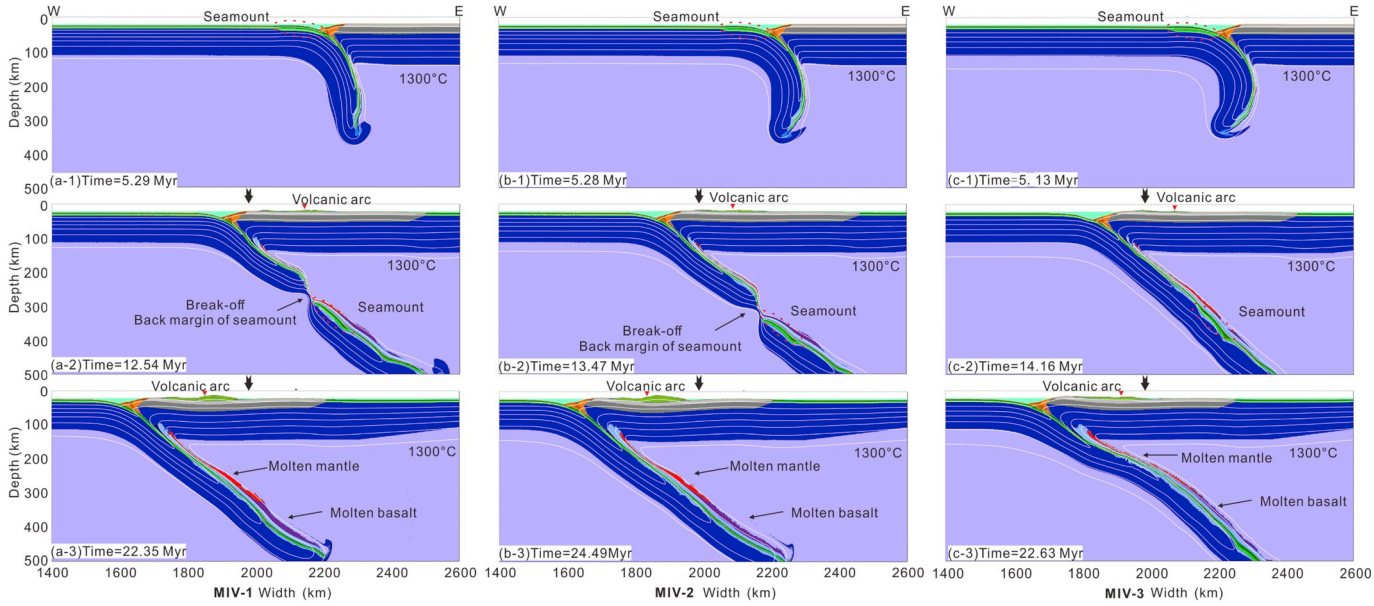

Fig. 9. Numerical modeling results with varied oceanic crust ages (MIV-1, MIV-2 and MIV-3). From (a) to (c), ages increases from 30 Ma to 40 Ma, and to 60 Ma, respectively.

with varying convergence rates before the occurrence of break-off (Table 3). All dip angles fall into a range of 32–45°, and a certain subducted slab length (500 km) is required for the occurrence of slab breakoff. This length is mainly controlled by upper plate motion, if other factors are constant. The slab break-off is also more likely to occur under continental overthrusting than oceanic subduction. Varying the overriding plate velocity does not change the break-off mode.

5.3. Slab age

The age of the subducting oceanic domain is another key parameter affecting the break-off process. The dynamic difference is mainly caused by variations in the temperature structure of the subducting oceanic plate (Gerya et al., 2004). With increasing oceanic age, the subducting slab becomes stronger and denser (Parsons and Sclater, 1977). In older slabs (which are also colder), more time is needed for thermal relaxation to increase the temperature and reduce slab viscosity.

Consistent with previous studies (Gerya et al., 2004; Andrews and Billen, 2009; Baumann et al., 2010), our results from models MIV-1 and MV-2 also show a positive correlation with the slab age, as well as the subducted slab length (< 60 Ma, Table 3), and the break-off of these weaker slabs is controlled by yielding strength within the slab interior (Andrews and Billen, 2009). The experiments of Baumann et al. (2010) indicate that a slab break-off event would occur even with the slab age is older than 100 Ma. However, our models show that break-off will not occur with a slab older than 60 Ma. This difference may be due to the different model set-ups. In the models of Baumann et al. (2010), oceanic subduction was followed by buoyant continental crust, which caused a slowdown of the oceanic subduction rate due to continent-continental collision, favoring the occurrence of break-off even with old slab age.

5.4. Role of the seamount

As a seamount or ridge approaches a trench, the tectonic coupling between converging plates increases (Gerya et al., 2009). Our results indicate that the break-off position is at either the front margin or the back margin of the seamount, which are the most favorable places for stress concentration. Previous numerical modeling have proved that lateral heterogeneities in the material geometries or properties influence the stress field, i.e., the stress concentrates on the position where larger variations are present (Kurek et al., 2014). In contrast, the result of MV-1 (model without a seamount) is characterized by a 2 Myr delay in the break-off time (13.98 Myr compared with the 10.72 Myr of the reference model), and subsequently by a flat subduction due to the hydrodynamic suction forces.

In 2D modeling the seamount is infinitely long parallel to the trench which causes a dimensional problem. However, our 2D modeling results are reconcilable with recent 3D modeling studies, in which a break-off/slab tear was also obtained by seamount subduction (Mason et al., 2010; Liu and Stegman, 2011; Taramón et al., 2015; Hu and Liu, 2016). By varying the densities of the buoyant plateaus, a slab tear formed in the subducted portion of the slab beneath plateaus soon after the slab dip reached the top of the lower mantle (Mason et al., 2010). Hu and Liu (2016) used the data assimilation algorithms to model the subduction history of South America since 100 Ma and obtained slab break-off at Nazca Ridge and Juan Fernandez Ridge. They suggested that the slab break-off/tear would be initiated by differential sinking rates between the subducting seamount and the surrounding slab portions (Gutscher et al., 1999). As the seamounts are generally more buoyant than the surrounding slab, they tend to sink slowly, which results in extensional stress accumulation around the front margin of the seamount (Hall and Spakman, 2015; Hu and Liu, 2016). This further supports our results that the seamount is a favorable locus for break-off. Because the strain required for break-off in our model is mainly induced by slab's pulling force, which depends on the subducted length. A buoyant feature difference along strike in a 3D modeling would enhance the extensional stain at the subducted seamount margin, which would promote the slab break-off.

In a 3D subduction modeling without a seamount, a trench-parallel buoyancy feature difference generally induces differential motion along the down dip and contributes to extensional stress within the slab, but it is not sufficient for slab break-off (Liu and Stegman, 2011). For example, sharp slab dip angle changes were achieved with a flat subduction instead of break-off due to a more distributed stress, which is originated from hydrodynamic suction due to a thick upper plat (Taramón et al., 2015; Hu and Liu, 2016). It seems that slab break-off requires extra extensional stress, i.e., higher localized dynamic pressure below the buoyant slab compared to the adjacent slab (Liu and Stegman, 2011). Since slab break-off was obtained in the MV-1 2D model, in which buoyancy was consistently parallel to the trench, a

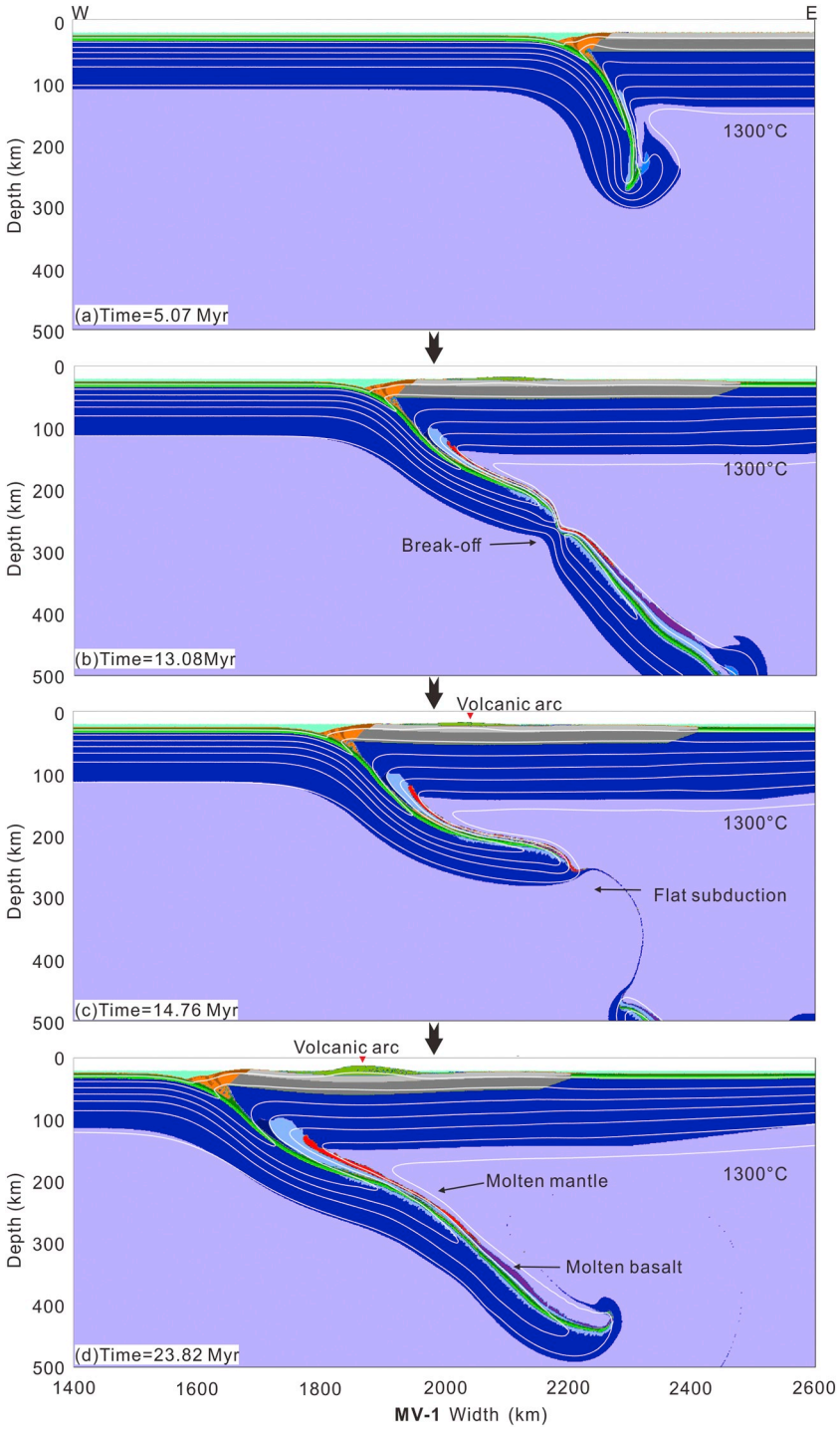

Fig. 10. Numerical modeling result without a seamount on the oceanic domain (MV-1).

lateral differential buoyancy in 3D will also promote slab break-off.

5.5. Partial melting and volcanic activities

It have been generally accepted that dehydration of subducted oceanic lithosphere will cause partial melting, and the molten migrates upward and drives arc magmatism at convergent plate margins (e.g. Schmidt and Poli, 1998; van Keken et al., 2011). As shown in our models, partial melting is more likely to occur with seamount subduction, since the seamount will not only bring in more water, but also increase the buoyance will shallows the dip angle of the subdcuting slab. The reverse cases are shown in MI-3 and MII-3, these models with a steep dip angle will cause rapid slab sinking, and thus hinder the increase in temperature of the subducted oceanic crust and sediments.

As mentioned above, seamount subduction will promote the occurrence of slab break-off. A slab break-off can account for magmatism through the formation of a slab window, subsequent heating of the overriding plate, and decompression melting of upwelling asthenosphere (Davies and von Blanckenburg, 1995; Freeburn et al., 2017). The increase in temperature of the subducted oceanic crust and sediments during slab necking and breakoff will also be sufficient to generate significant amounts of melt (Bouilhol et al., 2015). In most models with

the occurrence of slab break-off, especially for the MII model series with higher C (Fig. 5) and MIV model series with older slab age (Fig. 9), a single or a double volcanic arc could be observed due to slab melting. However, in the non-break-off model (MIV-3), the magmatism is much more limited (Fig. 9c-3). An exception is model MIII-4 with an extremely low convergence rate (1 cm/yr, Fig. 7b), where a volcanic arc is produced due to the long-lasting subduction. Our models also prove that slab break-off is likely to induce more volumes of melting, and thus enhance the intensity of magmatism.

5.6. Implications for seamount subduction at the Manila Trench

We compared the results of our numerical experiments with the subduction process of the Zhenbei-Huangyan Seamount, from which our approximate dimensions were chosen.

As shown in Fig. 1, the Zhenbei-Huangyan Seamount is subducting under the Manila Trench around 16° N. The Manila Trench has a length (extent parallel to trench) of ~1000 km (Schellart et al., 2007). Previous studies indicated that this seamount extends northeastwards and reaches to 17–18° N under Luzon Island (Yang et al., 1996; Bautista et al., 2001). They suggested that the seamount subduction initiated at 5 Ma according to geochemical analysis of the volcanic rocks, and a slab break-off was achieved at the present location. In our reference model, the seamount begins to subduct after around 4.9 Myr, and takes an additional 5.2 Myr before the occurrence of slab break-off (Fig. 3a, b). This break-off timing coincides with the 4–5 Myr timespan between the initial subduction of the seamount and the recent position under Luzon Island inferred by Yang et al. (1996) and Bautista et al. (2001).

A recent high-resolution P-wave seismic tomography (Fan et al., 2016), which was created by systematically picking the top and bottom of the descending Pacific Plate based on the maximum gradient of high-velocity anomalies in tomographic images, allows a comparison between the deep structure under the Manila Trench and our numerical results. The seismic structures under Luzon Island are shown in Fig. 11. In the P-wave tomography section along 17° N (Fig. 11a), a low-velocity zone exists at depths between 60 and 190 km, which is interpreted as an indicator of slab tearing (Fan et al., 2016). In our model results, we confirm that the seamount margin is a weak point favoring the occurrence of slab break-off. Thus, this slab tearing of the subducting SCS might have occurred at the front margin of the subducted Zhenbei-Huangyan Seamount Chain. When viewed in the reality of 3D, this break-off may develop into a hole (Hall and Spakman, 2015; Hu et al., 2016). Since the hole starts along the seamount margin, it would then propagate towards both sides (van Hunen and Allen, 2011). This could explain why there is no lower velocity zone at 19° N under the Manila Trench (Fig. 11b). Furthermore, the absence of the seamount during subduction will delay the onset of break-off by at least 2 Myr based on our results (Fig. 10b). Additionally, the oceanic crust at 19° N is ~7 Myr older than that at 17° N based on the recent oceanic crust dating studies (Li et al., 2015), which could also contribute to the delayed occurrence of break-off.

Seismic structures at either 17° N or 19° N under Luzon Island show a shallow slab angle (25–30°). Our modeling results imply that, instead of the slab age (Table 3, MIV series), a shallow dip angle only becomes established with a higher V_{act} of the mantle (Table 3, MI and MII series). Thus, we suggest that the mantle rheology under the SCS and Luzon Island is relatively strong.

6. Conclusion

We conducted a series of thermo-mechanical modeling experiments to evaluate the seamount subduction process and its role during subduction. The results of all these numerical modeling were then independently evaluated with constraints derived from the interpretation of geophysical data at the Manila Trench.

Our results show that seamount subduction during continental overthrusting would favor the occurrence of slab break-off. The break-off would generally occur more readily at the seamount margin where extensional strain accumulates. The slab break-off may expand into a hole in reality (3D). There will be a ~ 2 Myr delay in the break-off time when there is no seamount on the oceanic domain during continental overthrusting. In contrast, during a oceanic subduction where downgoing plate move faster than upper plate, the subduction is continuous and steady without break-off events. The slab will penetrate into the lower mantle or flatten at a depth of around 660 km.

There are two major factors controlling the break-off timing and depth. The first factor is the convergence rate. An overthrusting continental domain with a fast-moving rate will increase the amount of extension within the slab by pulling the upper portion ocean-ward, and causing intensive extensional stress within the slab. A slab break-off event will then occur at a depth of 100–300 km at the front or back margin of the seamount. A certain length of subducted slab (500 km) is required. With a decreased moving rate, the timing of the break-off event will be extended, even featured with slab necking events instead of break-off with extremely slow convergence rate (1 cm/yr). The second factor is the slab age. Young slabs (< 60 Ma) show a positive correlation with the timing of slab break-off; whereas older slabs (≥60 Ma), which are stronger and colder, achieves stable subduction.

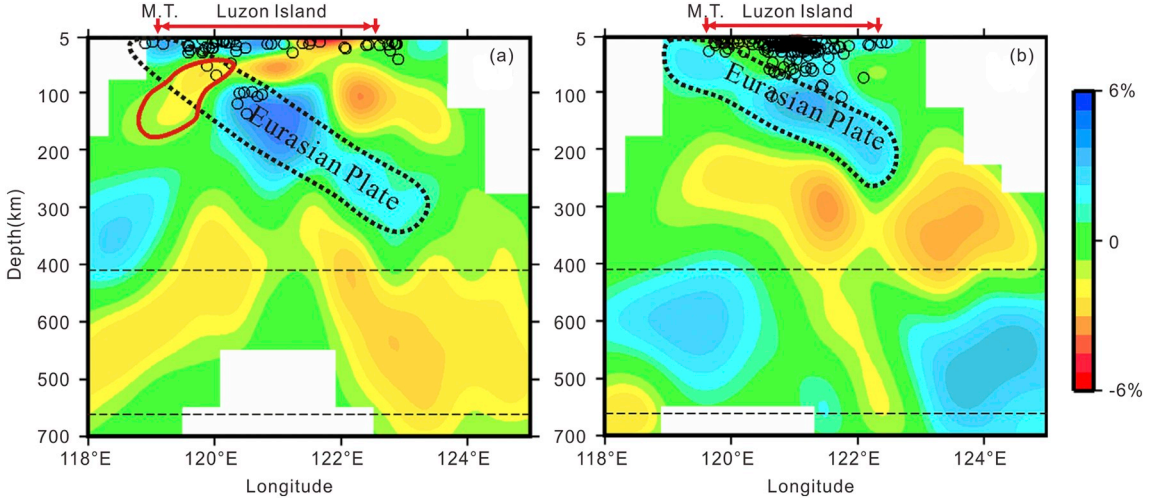

Fig. 11. Vertical cross sections of P-wave tomographic image across the Manila Trench. (See locations in Fig. 1). (a) Cross section along 17°N; (b) Cross section along 19°N. Modified from Fan et al., 2016.

Break-off events are not sensitive to rheology as indicated by V_{act} and C. A lower V_{act} of 0.8 will lead to a steep slab dip angle, and the slab will sink into the mantle more easily. While a lower C will result in more volumes of melting and magmatism.

With NNW-oriented overthrusting of the PSP above the EP in the SCS, the front of the Zhenbei-Huangyan Seamount Chain has been subducted under Luzon Island for ~5 Myr. We suggest that the low-velocity zone under Luzon Island revealed by the P-wave tomographic cross-section at around 17° N corresponds with a slab break-off event at the front of the Zhenbei-Huangyan-Seamount Chain, where a slab hole may have formed. Further to the north at about 19° N, the subducting oceanic slab is still continuous as revealed by the P-wave tomographic cross-section. The break-off event is delayed due to the absence of subducting seamounts and the older oceanic lithospheric age. The shallow dip angle of the subducting slab indicates relatively strong mantle rheology under the SCS and Luzon Island.

Acknowledgements

We are grateful to the anonymous reviewer for the constructive suggestions and fruitful comments for the manuscript. Dr. Lin Chen is thanked for his great help during modeling experiments, and Prof. Taras Gerya for his permission of thermo-mechanical code “I2VIS”. Funding for this research is provided by the National Key R&D Program of China (2016YFC0600402), State Oceanic Administration (SOA) global change and air–sea interaction special project (GASI-GEOGE-01), Natural Science Foundation of China (91858214, 41860811, 41676027, 41606051), and the NSFC-Shandong Joint Fund of Marine Science Research Centers (U1606401).

Appendix A. Supplementary data

Supplementary data to this article can be found online at https://doi.org/10.1016/j.tecto.2019.05.011.

References

Andrews, E.R., Billen, M.I., 2009. Rheologic controls on the dynamics of slab detachment. Tectonophysics 464 (1–4), 60–69. https://doi.org/10.1016/j.tecto.2007.09.004.

Baumann, C., Gerya, T.V., Connolly, J.a.D., 2010. Numerical modelling of spontaneous slab breakoff dynamics during continental collision. Geol. Soc. Lond., Spec. Publ. 332, 99–114. https://doi.org/10.1144/SP332.7.

Bautista, B.C., Bautista, M.L.P., Oike, K., Wu, F.T., Punongbayan, R.S., 2001. A new insight on the geometry of subducting slabs in Northern Luzon, Philippines. Tectonophysics 339 (3–4), 279–310. https://doi.org/10.1016/S0040-1951(01)00120-2.

Besana, G.M., Shibutani, T., Hirano, N., Ando, M., Bautista, B., Narag, I., Punongbayan, R.S., 1995. The shear wave velocity structure of the crust and uppermost mantle beneath Tagaytay, Philippines inferred from receiver function analysis. Geophys. Res. Lett. 22, 3143–3146. https://doi.org/10.1029/95GL03319.

Bittner, D., Schmeling, H., 1995. Numerical modeling of melting processes and induced diapirism in the lower crust. Geophys. J. Int. 123, 59–70. https://doi.org/10.1111/j.1365-246X.1995.tb06661.x.

Bouilhol, P., Magni, V., Van Hunen, J., Kaislaniemi, L., 2015. A numerical approach to melting in warm subduction zones. Earth Planet. Sci. Lett. 411, 37–44.

Briais, A., Patriat, P., Tapponnier, P., 1993. Updated interpretation of magnetic anomalies and seafloor spreading stages in the South China Sea: Implications for the Tertiary tectonics of Southeast Asia. J. Geophys. Res. Solid Earth 98 (B4), 6299–6328. https://doi.org/10.1029/92JB02280.

Clauser, C., Huenges, E., 1995. Thermal conductivity of rocks and minerals. In: Ahrens, T.J. (Ed.), Rock Physics and Phase Relations. AGU Reference Shelf 3. American Geophysical Union, Washington DC, pp. 105–126.

Crameri, F., Tackley, P.J., 2015. Parameters controlling dynamically self-consistent plate tectonics and single-sided subduction in global models of mantle convection. J. Geophys. Res. Solid Earth 120 (5), 3680–3706. https://doi.org/10.1002/2014JB011664.

Crameri, F., Tackley, P.J., Meilick, I., Gerya, T.V., Kaus, B.J.P., 2012. A free plate surface and weak oceanic crust produce single-sided subduction on Earth. Geophys. Res. Lett. 39 (3), 1–7. https://doi.org/10.1029/2011GL050046.

Davies, J.H., von Blanckenburg, F., 1995. Slab breakoff: a model of lithosphere detachment and its test in the magmatism and deformation of collisional orogens. Earth Planet. Sci. Lett. 129, 85–102.

Dimalanta, C.B., Yumul Jr., G.P., 2003. Magmatic and amagmatic contributions to crustal growth of an island arc system: the Philippine example. Int. Geol. Rev. 45, 922–935. https://doi.org/10.2747/0020-6814.45.10.922.

Ding, M., Lin, J., 2016. Deformation and faulting of subduction overriding plate caused by a subducted seamount. Geophys. Res. Lett. 43 (17), 8936–8944. https://doi.org/10.1002/2016GL069785.

Dominguez, S., Lallemand, S., Malavieille, J., Schnürle, P., 1998. Oblique subduction of the Gagua Ridge beneath the Ryukyu accretionary wedge system: Insights from marine observations and sandbox experiments. Mar. Geophys. Res. 20 (5), 383–402. https://doi.org/10.1023/A:1004614506345.

Dominguez, S., Malavieille, J., Lallemand, S.E., 2000. Deformation of accretionary wedges in response to seamount subduction: Insights from sandbox experiments. Tectonics 19 (1), 182–196. https://doi.org/10.1029/1999TC900055.

Duretz, T., Gerya, T.V., 2013. Slab detachment during continental collision: Influence of crustal rheology and interaction with lithospheric delamination. Tectonophysics 602, 124–140. https://doi.org/10.1016/j.tecto.2012.12.024.

Duretz, T., Gerya, T.V., May, D.A., 2011. Numerical modelling of spontaneous slab breakoff and subsequent topographic response. Tectonophysics 502 (1–2), 244–256. https://doi.org/10.1016/j.tecto.2010.05.024.

Elliott, T., Plank, T., Zindler, A., White, W., Bourdon, B., 1997. Element transport from slab to volcanic front at the Mariana arc. J. Geophys. Res. Solid Earth 102 (B7), 14991–15019. https://doi.org/10.1029/97JB00788.

Espurt, N., Funiciello, F., Martinod, J., Guillaume, B., Regard, V., Faccenna, C., Brusset, S., 2008. Flat subduction dynamics and deformation of the South American plate: Insights from analog modeling. Tectonics 27 (3), 1–19. https://doi.org/10.1029/2007TC002175.

Expedition 349 Scientists, 2014. South China Sea tectonics: Opening of the South China Sea and its implications for southeast Asian tectonics, climates, and deep mantle process since the late Mesozoic. In: International Ocean Discovery Program Preliminary Report, pp. 349. https://doi.org/10.14379/iodp.pr.349.2014.

Fan, J., Zhao, D., Dong, D., 2016. Subduction of a buoyant plateau at the Manila Trench: Tomographic evidence and geodynamic implications. Geochem. Geophys. Geosyst. 17 (2), 571–586. https://doi-org.libproxy.wlu.ca/10.1002/2015GC006201.

Ferrari, L., 2004. Slab detachment control on mafic volcanic pulse and mantle heterogeneity in central Mexico. Geology 32 (1), 77–80. https://doi.org/10.1130/G19887.1.

Franke, D., Savva, D., Pubellier, M., Steuer, S., Mouly, B., Auxietre, J.L., et al., 2014. The final rifting evolution in the South China Sea. Mar. Pet. Geol. 58 (B), 704–720. https://doi.org/10.1016/j.marpetgeo.2013.11.020.

Freeburn, R., Bouilhol, P., Maunder, B., Magni, V., van Hunen, J., 2017. Numerical model of the magmatic processes induced by slab beakoff. Earth Planet. Sci. Lett. 478, 203–213.

Gerya, T.V., Yuen, D.A., 2003. Rayleigh - Taylor instabilities from hydration and melting propel “cold plumes” at subduction zones. Earth Planet. Sci. Lett. 212 (1–2), 47–62. https://doi.org/10.1016/S0012-821X(03)00265-6.

Gerya, T.V., Yuen, D.A., 2007. Robust characteristics method for modelling multiphase visco- elasto-plastic thermo-mechanical problems. Phys. Earth Planet. Inter. 163 (1–4), 83–105. https://doi.org/10.1016/j.pepi.2007.04.015.

Gerya, T.V., Yuen, D.A., Maresch, W.V., 2004. Thermomechanical modelling of slab detachment. Earth Planet. Sci. Lett. 226, 101–116. https://doi.org/10.1016/j.epsl.2004.07.022.

Gerya, T.V., Fossati, D., Cantieni, C., Seward, D., 2009. Dynamic effects of aseismic ridge subduction: numerical modelling. Eur. J. Mineral. 21 (3), 649–661. https://doi.org/10.1127/0935-1221/2009/0021-1931.

Gorczyk, W., Willner, A.P., Gerya, T.V., Connolly, J.A.D., Burg, J., 2007. Physical controls of magmatic productivity at Pacific-type convergent margins: Numerical modelling. Phys. Earth Planet. Inter. 163, 209–232. https://doi.org/10.1016/j.pepi.2007.05.010.

Groome, W.G., Thorkelson, D.J., 2009. The three-dimensional thermo-mechanical signature of ridge subduction and slab window migration. Tectonophysics 464 (1–4), 70–83. https://doi.org/10.1016/j.tecto.2008.07.003.

Gutscher, M.-A., Olivet, J.-L., Aslanian, D., Eissen, J.-P., Maury, R., 1999. The “lost Inca plateau”: cause of flat subduction beneath Peru? Earth Planet. Sci. Lett. 171 (3), 335–341. https://doi.org/10.1016/S0012-821X(99)00153-3.

Hall, R., Spakman, W., 2015. Mantle structure and tectonic history of SE Asia. Tectonophysics 658, 14–45. https://doi.org/10.1016/j.tecto.2015.07.003.

Hawkesworth, C.J., Turner, S.P., Mcdermott, F., Peate, D.W., Calsteren, P. Van, 1997. U-Th isotopes in arc magmas: Implications for element transfer from the subducted crust. Science 276 (5312), 551–555.

He, E.Y., Zhao, M.H., Qiu, X.L., Sibuet, J.-C., Wang, J., Zhang, J.Z., 2016. Crustal structure across the post-spreading magmatic ridge of the East sub-basin in the South China Sea: Tectonic significance. J. Asian Earth Sci. 121, 139–152. https://doi:10.1016/j.jseaes.2016.03.003.

Hofmeister, A.M., 1999. Mantle values of thermal conductivity and the geotherm from phonon lifetimes. Science 283 (5408), 1699–1706. https://doi.org/10.1126/science.283.5408.1699.

Hsu, Y.J., Yu, S.B., Song, T.R.A., Bacolcol, T., 2012. Plate coupling along the Manila subduction zone between Taiwan and northern Luzon. J. Asian Earth Sci. 51, 98–108. https://doi.org/10.1016/j.jseaes.2012.01.005.

Hu, J., Liu, L., 2016. Abnormal seismological and magmatic processes controlled by the tearing South American flat slabs. Earth Planet. Sci. Lett. 450, 40–51. https://doi.org/10.1016/j.epsl.2016.06.019.

Hu, J., Liu, L., Hermosillo, A., Zhou, Q., 2016. Simulation of late Cenozoic South American flat-slab subduction using geodynamic models with data assimilation. Earth Planet. Sci. Lett. 438, 1–13. https://doi.org/10.1016/j.epsl.2016.01.011.

Huang, C.Y., Yuan, P.B., Tsao, S.J., 2006. Temporal and spatial records of active arc-continent collision in Taiwan: a synthesis. Bull. Geol. Soc. Am. 118 (3–4), 274–288. https://doi.org/10.1130/B25527.1.

Humphreys, E., 1995. Post-Laramide removal of the Farallon slab, western United States. Geology 23, 987–990. https://doi.org/10.1130/0091-7613(1995)023<0987:PLROTF>2.3.CO;2.
van Hunen, J., Allen, M.B., 2011. Continental collision and slab break-off: a comparison of 3- D numerical models with observations. Earth Planet. Sci. Lett. 302 (1–2), 27–37. https://doi.org/10.1016/j.epsl.2010.11.035.
van Hunen, J., Van Den Berg, A.P., Vlaar, N.J., 2000. A thermo-mechanical model of horizontal subduction below an overriding plate. Earth Planet. Sci. Lett. 182 (2), 157–169. https://doi.org/10.1016/S0012-821X(00)00240-5.
van Hunen, J., Van Den Berg, A.P., Vlaar, N.J., 2002. On the role of subducting oceanic plateaus in the development of shallow flat subduction. Tectonophysics 352 (3–4), 317–333. https://doi.org/10.1016/S0040-1951(02)00263-9.
Hutchison, C.S., 2010. The North-West Borneo Trough. Mar. Geol. 271, 32–43. https://doi.org/10.1016/j.margeo.2010.01.007.
Huw Davies, J., von Blanckenburg, F., 1995. Slab breakoff: a model of lithosphere detachment and its test in the magmatism and deformation of collisional orogens. Earth Planet. Sci. Lett. 129 (1–4), 85–102. https://doi.org/10.1016/0012-821X(94)00237-S.
Jian, Z., Larsen, H.C., Alvarez Zarikian, C.A., 2018. and the Expedition 368 Scientists. Expedition 368 Preliminary Report: South China Sea Rifted Margin. International Ocean Discovery Program. https://doi.org/10.14379/iodp.pr.368.2018.
van Keken, P.E., Hacker, B.R., Syracuse, E.M., Abers, G.A., 2011. Subduction factory: 4. Depth-dependent flux of H_2O from subducting slabs worldwide. J. Geophys. Res. 116, B01401. https://doi.org/10.1029/2010JB007922.
Koppers, A., 2014. On the 39Ar/40Ar dating of low-potassium ocean crust basalt from IODP expedition 349, South China Sea. In: AGU Fall Meeting, T31E-03. vol. 2014.
Koulakov, I., Wu, Y.M., Huang, H.H., Dobretsov, N., Jakovlev, A., Zabelina, I., Jaxybulatov, K., Chervov, V., 2014. Slab interactions in the Taiwan region based on the P- and S- velocity distributions in the upper mantle. J. Asian Earth Sci. 79, 53–64. https://doi.org/10.1016/j.jseaes.2013.09.026.
Kreemer, C., Holt, W.E., Haines, A.J., 2003. An integrated global model of present-day plate motions and plate boundary deformation. Geophys. J. R. Astron. Soc. 154 (1), 8–34.
Kurek, A., Niesłony, A., Kurek, M., 2014. Stress concentration resulting from irregular shape of explosively cladded materials connections - FEM simulation. Acta Mechanica et Automatica 8 (2), 103–106. https://doi.org/10.2478/ama-2014-0019.
Lallemand, S., Font, Y., Bijwaard, H., Kao, H., 2001. New insights on 3-D plates interaction near Taiwan from tomography and tectonic implications. Tectonophysics 335, 229–253. https://doi.org/10.1016/S0040-1951(01)00071-3.
Lallemand, S., Heuret, A., Boutelier, D., 2005. On the relationships between slab dip, back-arc stress, upper plate absolute motion, and crustal nature in subduction zones. Geochem. Geophys. Geosyst. 6 (9), 1–18. https://doi.org/10.1029/2005GC000917.
Li, C.F., Lin, J., Kulhanek, D.K., Williams, T., Bao, R., Briais, A., et al., 2014. Opening of the South China Sea and its implications for southeast Asian tectonics, climates, and deep mantle processes since the late Mesozoic. Integrated Ocean Drilling Program: Preliminary Reports. https://doi.org/10.2204/iodp.sp.349.2013.
Li, C.F., Li, J., Ding, W., Franke, D., Yao, Y., Shi, H., et al., 2015. Seismic stratigraphy of the central South China Sea basin and implications for neotectonics. J. Geophys. Res. Solid Earth 120, 1–23. https://doi.org/10.1002/2014JB011686.
Liu, L., Stegman, D.R., 2011. Segmentation of the farallon slab. Earth Planet. Sci. Lett. 311, 1–10. https://doi.org/10.10.1016/j.epsl.2011.09.027.
Livermore, R., Cunningham, A., Vanneste, L., Larter, R., 1997. Subduction influence on magma supply at the East Scotia Ridge. Earth Planet. Sci. Lett. 150, 261–275. https://doi.org/10.1016/s0012-821x(97)00074-5.
Manalo, P.C., Dimalanta, C.B., Faustino-eslava, D.V., Ramos, N.T., Queaño, K.L., Yumul, G.P., 2015. Journal of Asian Earth Sciences Crustal thickness variation from a continental to an island arc terrane: Clues from the gravity signatures of the Central Philippines. J. Asian Earth Sci. 104, 205–214. https://doi.org/10.1016/j.jseaes.2014.08.031.
Martinod, J., Funiciello, F., Faccenna, C., Labanieh, S., Regard, V., 2005. Dynamical effects of subducting ridges: Insights from 3-D laboratory models. Geophys. J. Int. 163 (3), 1137–1150. https://doi.org/10.1111/j.1365-246X.2005.02797.x.
Mason, W.G., Moresi, L., Betts, P.G., Miller, M.S., 2010. Three-dimensional numerical models of the influence of a buoyant oceanic plateau on subduction zones. Tectonophysics 483 (1–2), 71–79. https://doi.org/10.1016/j.tecto.2009.08.021.
McGeary, S., Nur, A., Ben-Avraham, Z., 1985. Spatial gaps in arc volcanism: the effect of collision or subduction of oceanic plateaus. Tectonophysics 119 (1–4), 195–221. https://doi.org/10.1016/0040-1951(85)90039-3.
Nikolaeva, K., Gerya, T.V., Connolly, J.A.D., 2008. Numerical modelling of crustal growth in intraoceanic volcanic arcs. Phys. Earth Planet. Inter. 171, 336–356. https://doi.org/10.1016/j.pepi.2008.06.026.
Parsons, B., Sclater, J.G., 1977. An analysis of the variation of ocean floor bathymetry and heat flow with age. J. Geophys. Res. 82 (5), 803–827. https://doi.org/10.1029/JB082i005p00803.
Qin, J.F., Lai, S.C., Li, Y.F., 2008. Slab Breakoff Model for the Triassic Post-Collisional Adakitic Granitoids in the Qinling Orogen, Central China: Zircon U-Pb Ages, Geochemistry, and Sr-Nd-Pb Isotopic Constraints. Int. Geol. Rev. https://doi.org/10.2747/0020-6814.50.12.1080.
Ranalli, G., 1995. Rheology of the Earth. Chapman and Hall, London.
Rosenbaum, G., Mo, W., 2011. Tectonic and magmatic responses to the subduction of high bathymetric relief. Gondwana Res. 19 (3), 571–582. https://doi.org/10.1016/j.gr.2010.10.007.
Schellart, W.P., Freeman, J., Stegman, D.R., Moresi, L., May, D., 2007. Evolution and diversity of subduction zones controlled by slab width. Nature 446, 308–311. https://doi.org/10.1038/nature05615.
Schmeling, H., 2006. A model of episodic melt extraction for plumes. J. Geophys. l Res. 111 (December 2005), 1–12. https://doi.org/10.1029/2004JB003423.
Schmeling, H., 2010. Dynamic models of continental rifting with melt generation. Tectonophysics 480 (1–4), 33–47. https://doi.org/10.1016/j.tecto.2009.09.005.
Schmidt, M.W., Poli, S., 1998. Experimentally based water budgets for dehydrating slabs and consequences for arc magma generation. Earth Planet. Sci. Lett. 163, 361–379. https://doi.org/10.1016/S0012-821X(98)00142-3.
Sella, G.F., Dixon, T.H., Mao, A., 2002. REVEL: a model for recent plate velocities from space geodesy. J. Geophys. Res. Solid Earth 107 (B4), 11–30. https://doi.org/10.1029/2000JB000033.
Sibuet, J.C., Yeh, Y.C., Lee, C.S., 2016. Geodynamics of the South China Sea. Tectonophysics 692, 98–119. https://doi:10.1016/j.tecto.2016.02.022.
Simons, W.J.F., Socquet, A., Vigny, C., Ambrosius, B.A.C., Abu, S.H., Promthong, C., et al., 2007. A decade of GPS in Southeast Asia: Resolving Sundaland motion and boundaries. J. Geophys. Res. Solid Earth 112 (6), 1–20. https://doi.org/10.1029/2005JB003868.
Sizova, E., Gerya, T., Brown, M., Perchuk, L.L., 2010. Lithos Subduction styles in the Precambrian: Insight from numerical experiments. Lithos 116 (3–4), 209–229. https://doi.org/10.1016/j.lithos.2009.05.028.
Sun, Z., Stock, J., Klaus, A., the Expedition 367 Scientists, 2018. Expedition 367 Preliminary Report: South China Sea Rifted Margin. International Ocean Discovery Programhttps://doi.org/10.14379/iodp.pr.367.2018.
Suppe, J., 1984. Kinematics of arc-continent collision, flipping of subduction, and back-arc spreading near Taiwan. Mem. Geol. Soc. China 6, 21–23.
Taramón, J., Rodríguez-González, J., Negredo, A., Billen, M., 2015. Influence of cratonic lithosphere on the formation and evolution of flat slabs: Insights from 3-D time-dependent modeling. Geochem. Geophys. Geosyst. 16, 2933–2948. https://doi.org/10.1002/2015GC005940.
Taylor, B., Hayes, D., 1983. Origin and history of the South China Sea basin. In: The Tectonic and Geologic Evolution of Southeast Asian Seas and Islands. Geophysical Monograph Series AGU.
Turcotte, D.L., Schubert, G., 2002. Geodynamics, 2nd edition. .
Vogt, K., Gerya, T.V., 2014. From oceanic plateaus to allochthonous terranes: numerical modelling. Gondwana Res. 25 (2), 494–508. https://doi.org/10.1016/j.gr.2012.11.002.
Wang, J., Zhao, M.H., Qiu, X.L., Sibuet, J.C., He, E.Y., Zhang, J.Z., Tao, C.H., 2016. 3D seismic structure of the Zhenbei–Huangyan seamounts chain in the East sub- basin of the South China Sea and its mechanism of formation. Geol. J. 51 (S1), 448–463. https://doi.org/10.1002/gj.2781.
Wang, Y.J., Han, X.Q., Luo, Z.H., Qiu, Y.Z., Ding, W.W., Li, J.B., Gao, S.T., Chen, R.H., 2009. Late Miocene magmatism and evolution of Zhenbei–Huangyan Seamount in the South China Sea: evidence from petrochemistry and chronology(in Chinese with English abstract). Acta Oceanol. Sin. 31 (4), 93–102. https://10.3321/j.issn:0253-4193.2009.04.011.
Wang, Z., Zhao, D., Wang, J., Kao, H., 2006. Tomographic evidence for the Eurasian lithosphere subducting beneath South Taiwan. Geophys. Res. Lett. 33, L18306. https://doi.org/10.1029/2006GL027166.
Wilmsen, M., Fürsich, F.T., Seyed-Emami, K., Majidifard, M.R., Taheri, J., 2009. The Cimmerian Orogeny in northern Iran: Tectono-stratigraphic evidence from the foreland. Terra Nova. https://doi.org/10.1111/j.1365-3121.2009.00876.x.
Wortel, M.J.R., Spakman, W., 2000. Subduction and slab Detachment in the Mediterranian- Carpathian region region. Science. https://doi.org/10.1126/science.290.5498.1910.
Wu, J., Suppe, J., Lu, R., Kanda, R., 2016. Philippine Sea and East Asian plate tectonics since 52 Ma constrained by new subducted slab reconstruction methods. J. Geophys. Res. Solid Earth (2), 6249–6262. https://doi.org/10.1002/2016JB012923.Received.
Yang, T.F., Lee, T., Chen, C.-H., Cheng, S.-N., Knittel, U., Punongbayan, R.S., Rasdas, A.R., 1996. A double island arc between Taiwan and Luzon: consequence of ridge subduction. Tectonophysics 258 (1–4), 85–101. https://doi.org/10.1016/0040-1951(95)00180-8.
Yoshioka, S., Wortel, M.J.R., 1995. Three-dimensional numerical modeling of detachment of subducted lithosphere. J. Geophys. Res. Solid Earth 100 (B10), 20223–20244. https://doi.org/10.1029/94JB01258.
Zhao, D., Yamamoto, Y., Yanada, T., 2013. Global mantle heterogeneity and its influence on teleseismic regional tomography. Gondwana Res. 23, 595–616. https://doi.org/10.1016/j.gr.2012.08.004.
Zhao, M., He, E., Sibuet, J.C., Sun, L., Qiu, X., Tan, P., Wang, J., 2018. Postseafloor spreading volcanism in the central east South China Sea and ts formation through an extremely thin oceanic crust. Geochem. Geophys. Geosyst. 19 (3), 621–641. https://doi.org/10.1002/2017GC007034.